




Ⓐ Microscale Updrafts within Northeast U.S. Coastal Snowstorms Using High-Resolution Cloud Radar Measurements

MARIKO OUE ^a, BRIAN A. COLLE,^a SANDRA E. YUTER,^b PAVLOS KOLLIAS,^{a,c} PHILLIP YEH,^a AND LAURA M. TOMKINS^b

^a *Stony Brook University, State University of New York, Stony Brook, New York*

^b *North Carolina State University, Raleigh, North Carolina*

^c *Brookhaven National Laboratory, Upton, New York*

(Manuscript received 13 March 2023, in final form 3 January 2024, accepted 5 January 2024)

ABSTRACT: Limited knowledge exists about ~100-m-scale precipitation processes within U.S. northeast coastal snowstorms because of a lack of high-resolution observations. We investigate characteristics of microscale updraft regions within the cyclone comma head and their relationships with snowbands, wind shear, frontogenesis, and vertical mass flux using high-spatiotemporal-resolution vertically pointing Ka-band radar measurements, soundings, and reanalysis data for four snowstorms observed at Stony Brook, New York. Updraft regions are defined as contiguous time–height plotted areas with upward Doppler velocity without hydrometeor sedimentation that is equal to or greater than 0.4 m s^{-1} . Most updraft regions in the time–height data occur on a time scale of seconds ($<20 \text{ s}$), which is equivalent to spatial scales $< 500 \text{ m}$. These small updraft regions within cloud echo occur more than 30% of the time for three of the four cases and 18% for the other case. They are found at all altitudes and can occur with or without frontogenesis and with or without snowbands. The updraft regions with relatively large Doppler spectrum width ($>0.4 \text{ m s}^{-1}$) occur more frequently within midlevels of the storms, where there are strong wind shear layers and moist shear instability layers. This suggests that the dominant forcing for the updrafts appears to be turbulence associated with the vertical shear instability. The updraft regions can be responsible for upward mass flux when they are closer together in space and time. The higher values of column mean upward mass flux often occur during snowband periods.

SIGNIFICANCE STATEMENT: Small-scale ($<500 \text{ m}$) upward motions within four snowstorms along the U.S. northeast coast are analyzed for the first time using high-spatiotemporal-resolution millimeter-wavelength cloud radar pointed vertically. The analysis reveals that updrafts appear in the storms regardless of whether snowbands are present or whether there is larger-scale forcing for ascent. The more turbulent and stronger updrafts frequently occur in midlevels of storms associated with instability from vertical shear and contribute to upward mass flux during snowband periods when they are closer together in space and time.

KEYWORDS: Snowbands; Turbulence; Precipitation; Snow

1. Introduction

Snowbands in the comma head of winter storms are responsible for much of the heavy snowfall over the northeast United States. Because of the large societal impacts of these winter storms, they have been studied for decades using both numerical models and observations (e.g., Novak et al. 2008; Stark et al. 2013; Plummer et al. 2014; McMurdie et al. 2022). These studies

have shown a spectrum of snowbands, ranging from single bands, which are defined as a single reflectivity feature $> 250 \text{ km}$ in length and $20\text{--}100 \text{ km}$ in width, with intensities of $>30 \text{ dBZ}$ maintained for at least 2 h, to smaller-scale multibands that occur in groups (Ganetis et al. 2018). The mechanisms that result in the variations in snowband characteristics are not well known.

Previous studies on snowband formation focused on the mesoscale ingredients of lift along a midlevel trough, instability, and moisture (Novak et al. 2010). While primary bands were often associated with midlevel frontogenesis (e.g., Novak et al. 2004, 2008), multibands were also associated with mesoscale instabilities, such as boundary layer instability, moist/conditional symmetric instability (e.g., Byrd 1989; Schultz and Schumacher 1999), conditional instability (e.g., Reuter and Yau 1990; Trapp et al. 2001; Morales 2008), and inertial instability (e.g., Jurewicz and Evans 2004; Schultz and

Ⓐ Denotes content that is immediately available upon publication as open access.

Corresponding author: Mariko Oue, mariko.oue@stonybrook.edu

DOI: 10.1175/MWR-D-23-0055.1

© 2024 American Meteorological Society. This published article is licensed under the terms of the default AMS reuse license. For information regarding reuse of this content and general copyright information, consult the AMS Copyright Policy (www.ametsoc.org/PUBSReuseLicenses).

Brought to you by North Carolina State University Hunt Library | Unauthenticated | Downloaded 06/03/24 02:18 PM UTC

Knox 2007). Earlier modeling and theoretical studies of multi-bands focused on the superposition of a frontogenetical circulation and either conditional instability or conditional symmetric instability (Xu 1992). However, Ganetis et al. (2018) showed that these bands often develop in a region of little or no frontogenesis; thus, other mechanisms may be responsible, such as elevated convection, generating cells, shear instabilities, and gravity wave activity, as well as microphysics, which often occur at smaller scales than frontogenesis and mesoscale instabilities (Bosart and Sanders 1986; Zhang et al. 2001, 2003; Kumjian et al. 2014; Plummer et al. 2014, 2015; Rauber et al. 2014, 2017; Rosenow et al. 2014, 2018; Keeler et al. 2016a,b, 2017; Kumjian and Lombardo 2017; Lackmann and Thompson 2019; McMurdie et al. 2022).

Snowbands also have variable microphysics that can impact precipitation rates. Studies using in situ surface measurements observed a variety of snowflake habits and degrees of riming within the cyclone comma head and storm evolution (e.g., Stark et al. 2013; Colle et al. 2014). In particular, the microphysical processes can change across the snowband from more rimed on the east (warmer) side to more dry snow on the west (colder) side. Those microphysical studies using in situ surface measurements have also revealed that upper-level cloud structures, dynamics, and microphysics (i.e., generating cells, turbulence) strongly impact the surface precipitation, while internal cloud processes can interact with each other producing complex microphysics. Field campaigns using high spatiotemporal resolution airborne radars [e.g., Profiling of Winter Storms (PLOWs); e.g., Rauber et al. 2014] revealed microscale convective updrafts producing generating cells, which contributed to greater ice production by vapor diffusion, riming, and aggregation processes (Plummer et al. 2014). Kumjian and Lombardo (2017) observed planar crystal growth and precipitation-type transitions (snow/rain/ice) in snowbands using the dual-polarization capabilities from the WSR-88D radar network. They also found a signature of secondary ice production. Those detailed, complex microphysical evolution in winter storms might not be captured by regional models (e.g., the Rapid Refresh model reanalysis with 50 vertical levels and 13-km horizontal grid spacing; Kumjian and Lombardo 2017) and even by cloud resolving models, likely due to deficiencies in many of the bulk microphysical schemes for winter storms (e.g., Naeger et al. 2017, 2020; Molthan et al. 2016). Motivated by those gaps in understanding microphysics and less representativeness in numerical models, the field campaign, the Investigation of Microphysics and Precipitation of Atlantic Coast-Threatening Snowstorms (IMPACTS; McMurdie et al. 2022) focuses on improving the understanding of snowfall processes, remote sensing of snow, and the prediction and evolution of banded structures. The campaign achieved multiscale observations including in situ and vertically pointing and scanning remote sensing measurements from both airborne and ground-based platforms.

Previous observational studies (e.g., Plummer et al. 2015; Rauber et al. 2014, 2017) corroborated the importance of turbulence to generate ice particles and intensify snowfall. Turbulence often has been observed by fine-scale Doppler radar observations to occur in multiple layers within stratiform snow clouds with frequent periodic upward-downward patterns within stratiform precipitation clouds without terrain forcings (e.g., Rauber et al.

2017). The upward motions could contribute to supply water vapor and hence further ice formation and/or growth resulting in generating cells (Kumjian et al. 2014) and intensifications of snow fallstreaks (Plummer et al. 2015; Rauber et al. 2017), as shown by prominent radar reflectivity compared to the background. One of the common factors that generate instability and turbulence in stratiform clouds is wind shear (i.e., Kelvin-Helmholtz instability). Previous studies such as Boucher et al. (1965), Wexler et al. (1967), and Syrett et al. (1995) observed wind shear varying in time in winter storms using Doppler radar measurements and suggested that the wind shear could play a role in the formation of generating cells. Rauber et al. (2014) revealed multiple sources of air masses with different wind directions and humidity associated with a comma head snowstorm. The multiple air masses controlled cloud structure including cloud depth, instability, and vertical wind shear and produced cloud-top turbulence and generating cells. Despite the importance of generating cells, as well as turbulence that contributes to vertical air motion, for snowfall intensification, the formation process of the turbulent layers and the roles in snowfall formations are still unclear. Such turbulence structures are usually not resolved by either regional models or operational radars.

In this study, we hypothesize that 1) this upward motion associated with fine-scale turbulence contributes to snowband formation and 2) the turbulence producing the updrafts is generated by wind shear and/or thermodynamic instability in association with Kelvin-Helmholtz instability. Particularly we investigate (i) frequency of upward motion component of fine-scale turbulence during the individual storms, (ii) contribution of the updrafts to the upward mass transport, (iii) relationships among the fine-scale upward motion, wind shear, and thermodynamic stability, and mesoscale forcing for ascent (e.g., frontogenesis).

The Ka-band Scanning Polarimetric Radar (KASPR) is an ideal remote sensing instrument to study the fine-scale kinematic and microphysical characteristics of winter storms (e.g., Oue et al. 2017; Kollias et al. 2020). KASPR has been part of the Stony Brook University and Brookhaven National Laboratory Radar Observatory (SBRO) since 2017 and is installed at the Stony Brook University site (Fig. 1). KASPR polarimetric and Doppler capabilities have revealed fine-scale dynamical and microphysical features within winter storms (Kumjian et al. 2020; Lamer et al. 2021; Oue et al. 2021).

This study uses data from four winter storms and focuses on characteristics of microscale (<1 km) updraft regions, their relationship with ambient conditions, and their role in vertical mass transport. Section 2 describes the datasets used in this study. Section 3 summarizes the meteorological context and evolution of the four events and the corresponding KASPR observations. The relationships among the observed updraft structures, precipitation features, and other storm parameters important for forcing for ascent (e.g., frontogenesis, Pettersen 1956) and wind shear are discussed in section 4. Finally, summary and conclusions are presented in section 5.

2. Data and methods

a. KASPR

KASPR is a state-of-the-art 35-GHz cloud scanning radar with a beamwidth of 0.32°, capable of collecting reflectivity, Doppler

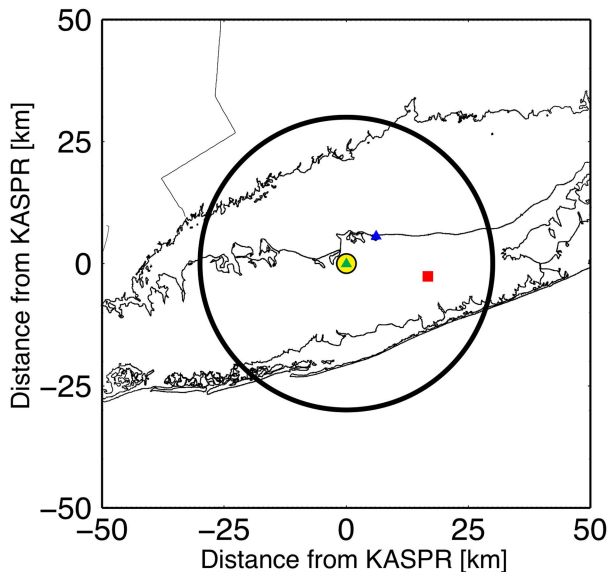


FIG. 1. Locations of KASPR (the center of this display, yellow dot), the nearest NWS sounding site (OKX, red square), and two SBU mobile sounding sites (SBU by green triangle and Cedar Beach by blue triangle). A large circle represents the KASPR's 30-km-radius maximum observation range.

velocity, Doppler spectrum width, and the standard set of polarimetric radar variables. The KASPR power measurements are calibrated using a corner reflector technique. The detailed specification of KASPR is available in Kumjian et al. (2020) and Kollias et al. (2020).

During winter storm observations, KASPR executed a scanning strategy that consisted of a plan position indicator (PPI) surveillance scan at 15° elevation angle (and 20° for the 2018 winter), a zenith-pointing (90° elevation angle) PPI for calibration, horizon-to-horizon range–height indicator (RHI; Kollias et al. 2014) scans, and a vertically pointing mode (VPT). Following Kumjian et al. (2020), this pattern was repeated and took approximately 13–15 min to complete, providing the slant PPI surveillance scans every 7 min (15 min for the 2018 winter). RHI scans crossing and/or along the snowbands were performed in each cycle producing RHI scans toward the same direction every 40 s to 3.5 min (40 s to 15 min for the 2018 winter). The PPI and RHI scans were performed with a full polarimetry mode and scan speeds of 6° and 2° s^{-1} , respectively, to collect data with a 30-m range-gate spacing, 0.6° PPI azimuthal spacing, and 0.3° RHI elevation spacing. The VPT mode was executed with only horizontally polarized waves transmitted and both horizontally and vertically polarized waves received. The KASPR radar was in VPT mode for consecutive periods lasting 2–5 min with a 15-m range-gate spacing. Based on the beamwidth, the horizontal resolution at a 10-km range is approximately 56 m. This study did not apply attenuation corrections for hydrometeors, and carefully selected periods when ice precipitation dominates through the cloud to avoid significant attenuation by liquid precipitation. If the column included liquid precipitation signatures, which could be defined by the presence of melting layer(s) in the VPT measurements, the column is excluded from the analysis.

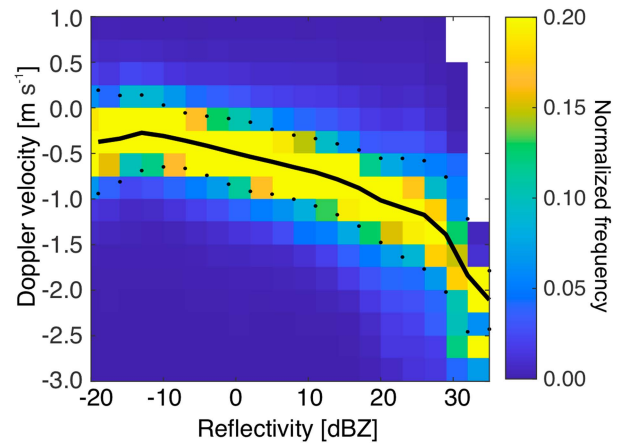


FIG. 2. Reflectivity vs Doppler velocity from all KASPR VPT data used in this study from the selected four cases. Color shade represents frequency normalized every 3 dB. Solid and dotted lines represent median Doppler velocity every 3 dB and median Doppler velocity plus and minus one standard deviation, respectively. Negative Doppler velocity values indicate downward motion. Doppler velocity is scaled for air density using the nearest sounding data.

The VPT measurements were used to identify updraft regions (URs) in time–height plots based on Doppler velocity. First, Doppler velocity with reflectivity < -20 dBZ was removed from the analysis since it was too noisy. Then the hydrometeor sedimentation component (i.e., fall speed) was removed from the measured Doppler velocity following Protat and Williams (2011) using reflectivity versus Doppler velocity (Z – V) relationships. In this study, the hydrometeor fall speed was estimated as the median Doppler velocity for every 3 dB from -20 to 34 dBZ, assuming that the mean vertical air motion for a certain time period at a given height was $\sim 0 \text{ m s}^{-1}$. Whenever >100 samples were available in a bin and median Doppler velocity was negative, we estimated the Z – V relationship every 500 m using hourly VPT data and used the median value of Doppler velocity as the hydrometeor fall speed at each Z bin at each height–hour window. For bins with few observations (<100 samples) or a positive median Doppler velocity (ascent), we instead used the statistical value of the median Doppler velocity estimated from all VPT data shown in Fig. 2 (black line) as the hydrometeor fall-speed estimate. To avoid accounting for range gates not representing updrafts due to the variability of the Doppler velocity, we considered updraft regions to be range gates where the measured Doppler velocity minus the estimated hydrometeor fall speed was greater than equal to 0.4 m s^{-1} . The threshold of 0.4 m s^{-1} is the value of standard deviation of Doppler velocity in Fig. 2. For example, in Fig. 2, for -1 dBZ the estimated fall speed is -0.48 m s^{-1} so measured Doppler velocity values $> -0.08 \text{ m s}^{-1}$ are considered to be updrafts. For 20 dBZ the estimated fall speed is -1.01 m s^{-1} so measured Doppler velocity values $> -0.61 \text{ m s}^{-1}$ are considered updrafts. We defined the UR as a region with at least 15 updraft range gates connected in time or height. Small regions having less than 15 range bins are removed from the analysis.

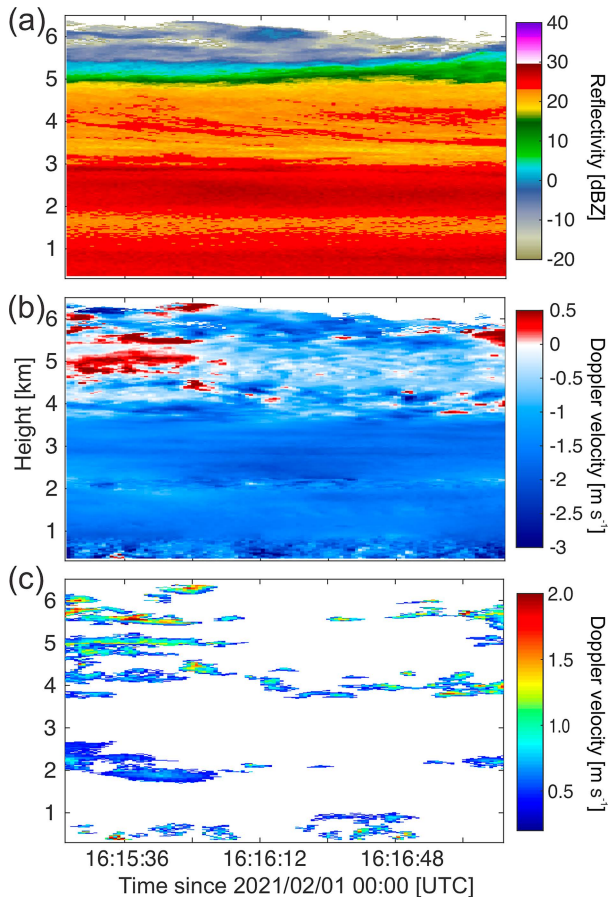


FIG. 3. Height-vs-time cross sections of (a) KASPR reflectivity and (b) Doppler velocity from vertically pointing measurements from 1615:18 to 1620:10 UTC 1 Feb 2021, and (c) the estimated upward vertical air motion $> 0.4 \text{ m s}^{-1}$ (estimated after removing hydrometeor fall speed from the measured Doppler velocity). Very small updraft regions < 15 range bins are not included in the analysis.

Figure 3 shows an example of 5-min VPT reflectivity (Fig. 3a), Doppler velocity (Fig. 3b), and the identified updrafts from 1615:18 UTC for 5 min on 1 February 2021. We tested other Doppler velocity thresholds (0.0 and 0.6 m s^{-1}) that were applied to the Doppler velocity after the sedimentation (i.e., fall speed) removal and confirmed that varying the threshold within this range had little impact on the results. For example, when the threshold is increased from 0.4 to 0.6 m s^{-1} , the total number of URs decreases by 28% – 49% ; however, the shapes of the normalized size distribution (discussed in section 4) and vertical distribution do not change. Because of the uncertainty of the detected numbers of URs that depend on the thresholds, the analysis in this study focuses on qualitative descriptions rather than quantitative discussion.

The duration of the detected URs is the time between the earliest and latest times of the appearance of the UR region. The vertical extent is the height between the lowest and highest range bins of the appearance of the region. The altitude of individual updraft regions is estimated as a mean of altitudes

of range gates in the updraft regions (Fig. 3c). Fine-scale turbulence can contribute to Doppler spectrum width (SW; appendix). For the VPT measurements using the narrow beamwidth (0.3°) in this study, the wind shear component in the observed SW would be mostly dominated by horizontal/vertical gradients in vertical air motion within the radar range gate. We use $\text{SW} > 0.4 \text{ m s}^{-1}$ from the VPT measurements to represent the fine-scale turbulence (appendix). The Doppler spectrum width (SW) from the VPT measurements is averaged in each UR.

To understand the role of URs on snowfall intensification, we estimate the upward mass flux based on the detected URs. The bulk mass flux (MF) at each altitude can be estimated as

$$\text{MF} = \overline{W} \rho_d U F \quad (\text{kg m}^{-2} \text{ s}^{-1}), \quad (1)$$

where \overline{W} is the mean updraft that is the positive Doppler velocity from the detected updraft regions averaged over time at each altitude, ρ_d is the dry air density estimated from the nearest-time sounding measurements, and UF is the updraft fraction estimated as the ratio of the time of updraft (positive Doppler velocity in the detected updraft regions) to the total cloudy time for each VPT file (bulk mass flux). The mass flux profile from each VPT file is then averaged $> 1.2 \text{ km}$ above ground level (AGL) for each VPT file (column mean mass flux).

Because we highlight the importance of shear-driven turbulence, we compute vertical wind shear, which measures the likelihood of turbulence. The Kelvin–Helmholtz instability can appear when the Richardson number is small ($< \sim 0.25$). Here we introduce the moist Richardson number (mRi) to represent the instability in this cloudy environment. First, we estimate wind direction and speed from KASPR PPI measurements at an elevation angle of 15° (approximately every 7 min) using a velocity–azimuth display (VAD) technique (Browning and Wexler 1968). Using the VAD data up to maximum height of 7.8 km AGL, we estimated the vertical wind shear (V_{shear}):

$$V_{\text{shear}} = \sqrt{(u_{z_2} - u_{z_1})^2 + (v_{z_2} - v_{z_1})^2} / (z_2 - z_1), \quad (2)$$

where z represents height and u_z and v_z represent horizontal wind components at z . We use a 100 m (124 m for the 4 January case) spacing to estimate V_{shear} at each VAD data point ($z_2 - z_1 = 100 \text{ m}$). Since only a single elevation angle is used for the VAD, the resulting horizontal wind profile is based on an increasing diameter cone with increasing height ($\sim 7.5\text{-km}$ diameter for 1-km altitude and $\sim 59.7 \text{ km}$ for 8-km altitude). The mRi is calculated using the following equation (Markowski and Richardson 2010):

$$\text{mRi} = \frac{N_m^2}{\left(\frac{\Delta u}{\Delta z}\right)^2 + \left(\frac{\Delta v}{\Delta z}\right)^2}. \quad (3)$$

The Brunt–Väisälä frequency N_m is defined as

$$N_m = \sqrt{\frac{g}{\theta_e} \frac{\Gamma_m}{\Gamma_d} \frac{\Delta \theta_e}{\Delta z}}, \quad (4)$$

where θ_e is equivalent potential temperature, Γ_d and Γ_m are dry adiabatic lapse rate and pseudo adiabatic lapse rate,

respectively, and g is Earth's gravity. Values of θ_e and Γ_m were estimated from the nearest soundings. Horizontal wind components u and v can be obtained from soundings or the KASPR VAD measurements. A Δz of 100 m (124 m for the 4 January case) was used in this study. Γ_m was estimated using the following equation (Markowski and Richardson 2010):

$$\Gamma_m = \frac{g + \frac{dL_v r_v}{dz}}{c_{pd} + r_v c_l}, \quad (5)$$

where L_v is the latent heat of vaporization, r_v is the water vapor mixing ratio, c_{pd} is the specific heat of dry air at constant pressure, and c_l is the specific heat capacity of liquid water.

b. Sounding and WSR-88D radar data

Twice-daily radiosonde data at 0000 and 1200 UTC were used from the nearest NWS site (OKX; red square in Fig. 1), which is ~22 km to the east of Stony Brook. For the events in 2020 and 2021 additional soundings were launched every ~3 h using the GRAW sounding system installed on a Stony Brook University (SBU) mobile radar truck. The SBU mobile radar truck was deployed in several locations in Long Island including Cedar Beach (40.965°N, -73.030°E; blue triangle in Fig. 1; for 18 January 2020) and Stony Brook University (40.897°N, -73.127°E; green triangle in Fig. 1; for 17 December 2020 and 1 February 2021).

To provide the regional precipitation context for these snow events, we used the radar reflectivity from the NEXRAD WSR-88D surveillance scans at the lowest two elevation angles (i.e., 0.5° and 0.8°) at the KOKX site.

c. Reanalysis data

The Rapid Refresh reanalysis (RAP; Benjamin et al. 2016) was used to examine the environment and frontogenesis during the snowstorm events. It uses hourly updated data assimilation with 37 pressure levels and 13.5-km grid spacing.

The mean sea level pressure from the fifth generation of the European Centre for Medium-Range Weather Forecasts (ERA5; Hersbach et al. 2020) was used to track cyclone centers. It provides hourly data interpolated into 37 pressure levels at 0.25° grid spacing. The cyclone tracking was based on the mean sea level pressure value less than 1010 hPa, gradients of the mean sea level pressure, and the distance from the previous cyclone center, following Crawford et al. (2021).

d. Snow events

We examined four snowstorm cases: 4 January 2018, 18 January 2020, 16–17 December 2020, and 31 January to 1 February 2021. Three cases (4 January 2018, 16–17 December 2020, and 31 January–1 February 2021) had multibands, while the other case (18 January 2020) included a primary band (Table 1). The tracks of the surface low pressure centers for the storms are shown in Fig. 4. The cases were chosen to provide a diverse set of band structures within the cyclone comma head. Table 1 summarizes the storm characteristics and sample size for each case. Brief descriptions of the cases and synoptic conditions will be shown in section 3b.

TABLE 1. Summary of the storm characteristics and sample sizes. Soundings at 0000 and 1200 UTC are from the NWS OKX soundings, and the others are from the SBU mobile truck.

Date	Storm quadrant	Types of bands within storm	Trend in storm Z intensity as it passed over Stony Brook (based on NEXRAD)	Period	Total cloudy time analyzed by VPT (min)	No. of VPT files used	No. of VAD profiles (PPI data files) used	Sounding times
4 Jan 2018	S	Multibands	Sustain Z > 30 dBZ	1009–2355 UTC	278.2	56	138	1200 UTC 4 Jan, 0000 UTC 5 Jan
18 Jan 2020	NW to W	Single band	Weaken from 30 to <25 dBZ	1410–2359 UTC	196.7	80	80	1200 UTC 18 Jan, 1800 UTC 18 Jan, 1900 UTC 18 Jan, 2100 UTC 18 Jan, 0000 UTC 19 Jan
16–17 Dec 2020	N to NW	Multibands	Sustain Z > 30 dBZ	1822 UTC 16 Dec–0259 UTC 17 Dec	184.1	75	76	1200 UTC 16 Dec, 0000 UTC 17 Dec, 0300 UTC 17 Dec
31 Jan–1 Feb 2021	N	Multibands	Weakening from 40 to 30 dBZ	1802 UTC 31 Jan–2351 UTC 1 Feb	236.4	119	170	1200 UTC 31 Jan, 0000 UTC 1 Feb, 0600 UTC 1 Feb, 0800 UTC 1 Feb, 1200 UTC 1 Feb, 1500 UTC 1 Feb, 1800 UTC 1 Feb, 2100 UTC 1 Feb, 0000 UTC 2 Feb

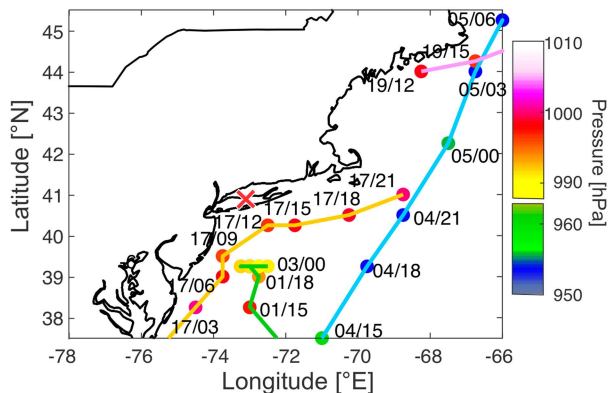


FIG. 4. Tracks of the cyclone centers every 3 h using ERA5 mean sea level pressure for the cases of 4 Jan 2018 (blue line), 18 Jan 2020 (magenta line), 17–16 Dec 2020 (orange line), and 31 Jan–1 Feb 2021 (green line). The color for each dot represents the surface central pressure (in hPa) every 3 h. Cross mark represents the Stony Brook location.

3. Results

a. Characteristics of detected updraft regions

Table 2 lists the number of the URs detected within the cloud echo observed by the KASPR VPT measurements, and those normalized by the total cloudy time per 5 min (number per 5 min), which is defined as an accumulated time where KASPR observed cloud echoes at any altitude during the analysis period. The warm frontal band case on 18 January 2020 has the lowest number of the updraft regions per 5 min among the four cases (~10 regions per 5 min). The other cases have 2–5 times more URs.

We identified the URs below ~1.2 km AGL for all cases. These are likely associated with the boundary layer turbulence. To focus on updrafts that may have strong relationships with storm evolution, wind shear, and shear-induced turbulence in clouds, we do not include the boundary layer updraft regions in the present analysis. The height of the planetary boundary layer (PBL) was determined as the bottom of the temperature inversion layer near the surface using the sounding profiles. They are 0.5 km for 4 January, 0.9 km for 18 January, 1.1 km for 16–17 December, and 0.7 km for 1 February 2021. The numbers of URs above the PBL are also listed in Table 2.

Figure 5a shows frequency distributions of the duration of URs detected above the PBL within a 10-s interval. Even though the

number of detected URs varies by event, the qualitative characteristics of the duration time distribution are similar for all four cases. There is a peak at the smallest size bin for the four cases, and overall, the number exponentially decreases with size. Most of the updraft regions last for less than 20 s (i.e., small size in the height–time plots), accounting for approximately 80% of the total. The maximum duration bin is 95 s. This distribution shape and qualitative features do not change when different thresholds are used for Doppler velocity (section 2a). The distribution curves from the three cases that had more than 1700 updraft regions show similar exponential distribution. Considering that the horizontal extent of UR can be roughly estimated as duration × horizontal wind speed estimated from the KASPR VAD, approximately 85% of URs have the horizontal scale < 500 m. It is highly possible that portions of the URs passed through the radar site rather than the part of the maximum dimensions and the horizontal scale could be an underestimate. Although it is difficult to estimate URs using the tilted scans, the KASPR RHI measurements showed cell-like features with horizontal scale < 500 m. The mean vertical extent of URs from the VPT measurements is 261 m for all cases, and more than 81% of URs have vertical extents less than 330 m. The aspect ratio of the URs (defined as the ratio of the horizontal scale to the vertical extent) for each case shown in Fig. 5b has a lognormal frequency distribution with the frequency peak around 1 (i.e., circular).

Table 3 summarizes the characteristics of the detected URs for each case. The URs have a median vertical extent of 150–240 m. We classified the regions for smaller and larger SW from the KASPR VPT measurements with a threshold of 0.4 m s⁻¹; UR with SW < 0.4 m s⁻¹ named URSWLO and UR with SW > 0.4 m s⁻¹ named URSWHI. Higher values of SW > 0.4 m s⁻¹ can be a proxy for higher magnitudes of turbulence (appendix). The URSWHIs are thicker than URSWLOs for all cases, but the difference varies between 0 m (16–17 December) and 90 m (18 January). Considering the range-gate spacing for the VPT measurements, the difference in the number of range gates for the vertical extent is less than 6. These qualitative characteristics do not change significantly when the Doppler velocity threshold for the detection is changed to 0.2 and 0.6 m s⁻¹.

b. Spatial distributions of updraft regions

1) 4 JANUARY 2018

At 1200 UTC 4 January 2018, a deep surface cyclone (~968 hPa) was located a few hundred kilometers to the southeast of Long Island, New York. As the storm center moved from south of

TABLE 2. The number of detected updraft regions in total and normalized per 5 min (number per 5 min). The numbers of detected updraft regions counted for heights above the PBL are also listed. The percentages in the parenthesis in the rightmost column represents those of the total number of URs for height above the PBL.

	Total number	Above PBL	Average per 5 min	Normalized number per 5 min above PBL	Number with SW > 0.4 m s ⁻¹ for height above PBL
4 Jan 2018	3376	2923 (86.6%)	60.7	52.5	1142 (39.1%)
18 Jan 2020	673	517 (76.8%)	17.2	13.2	21 (4.1%)
16–17 Dec 2020	2774	2311 (83.3%)	75.3	62.8	667 (29.9%)
31 Jan–1 Feb 2021	2171	1728 (79.6%)	45.9	36.5	542 (31.4%)

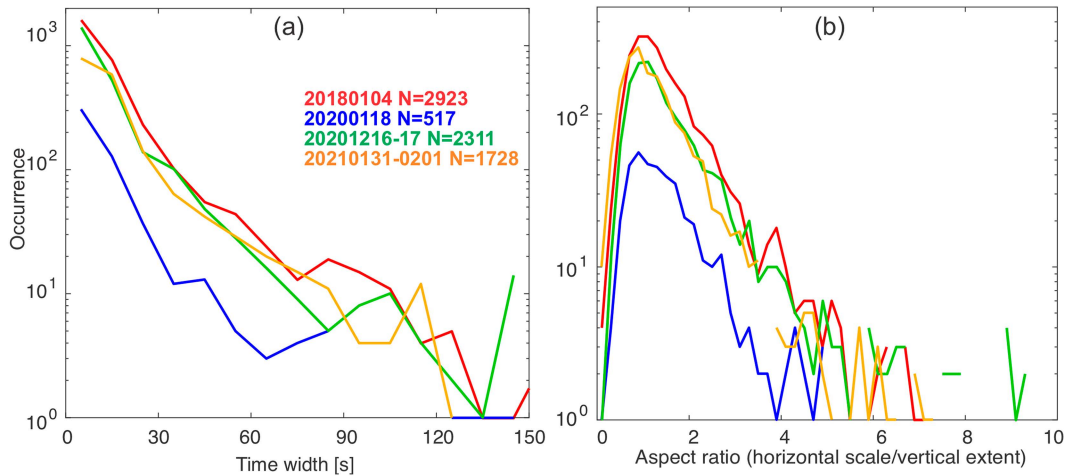


FIG. 5. Distributions of (a) time-width of the URs with the time bin size of 10 s for 4 Jan 2018 (red), 18 Jan 2020 (blue), 16–17 Dec 2020 (green), and 31 Jan–1 Feb 2021 (orange) and (b) aspect ratio of the URs defined as the ratio of horizontal scale to the vertical extent with the aspect ratio bin size of 0.2. The time width for each updraft region is defined as the time between the time when the updraft region appeared first and the time when it disappeared. The horizontal scale is estimated using the time width and the horizontal wind speed estimated from the KASPR VAD measurements. The sample size for each case is shown in the right corner in (a).

Long Island to the northeast (blue track in Fig. 4), the snowbands within the comma head produced heavy snow across Long Island from 1000 UTC 4 January to 0100 UTC 5 January 2018. Figure 6 shows the horizontal distributions of the NEXRAD reflectivity at the time of snowbands, 700 hPa RAP, and the 1200 UTC sounding profile. From 0900 to 1730 UTC, narrow snowbands (to 25 dBZ) orientated north-northeast to south-southwest crossed SBU (Fig. 6a), about 300 km northwest of the surface cyclone (Fig. 4). The snowband pivoted and changed its motion from westward to eastward around 1730 UTC, as the cyclone center moved ~500 km southeast of Long Island. The snowbands passed over SBU from west to east around 2030–2100 UTC. After the passage of the snowband, several relatively weak reflectivity bands < 25 dBZ, oriented along north-to-south or north-northwest-to-south-southeast passed through SBU until 0200 UTC 5 January 2018. At 700 hPa (Fig. 6b), southeasterly wind with the closed low resulted in warm advection extending northward to Long Island, likely producing vertical wind shear.

The NWS sounding at 1200 UTC 4 January shows a gradual wind veering from northeasterly below 2.5 km above mean sea level (MSL) to southerly at 6 km MSL (Fig. 6c), while there was a stable layer with a shallow frontal zone from 0.4 to 0.8 km MSL. From Eq. (2), there were relatively large vertical wind shear layers (>15 m s⁻¹ km⁻¹) below 6 km MSL (e.g., 0.8, 1.3, 1.9, 3.5, 4.6, and 5.7 km; Fig. 6c). They generally corresponded to heights of positive gradient of temperature (black line) and θ_e (blue solid line), and a few of them corresponded to the $mRi < 0.25$ (indicated by gray shades in Fig. 6c).

Figure 7 shows vertical cross sections of the snowbands from the KASPR RHI and height-versus-time plots during the snowband from the VPT measurements. The KASPR RHI measurements across the snowbands at 1432 UTC (135° in azimuth; Figs. 7a–c) reveal individual cells between 4- and 7-km altitudes and fallstreaks underneath. The KASPR reflectivity and Doppler velocity from the VPT measurements (Figs. 7d,e) also reveal updrafts in the convective cell layer and the fallstreaks attaining the 30-dBZ reflectivity. This convective cell layer at

TABLE 3. Median duration, vertical extent, maximum upward motion (maximum Doppler velocity without estimated fall speed in each UR), and reflectivity from the KASPR VPT moments for UR with $SW > 0.4 \text{ m s}^{-1}$ (URSWHI) and $SW < 0.4 \text{ m s}^{-1}$ (URSWLO) found at heights > 1.2 km.

	Median duration (s)		Median vertical extent (m)		Median maximum upward motion (m s^{-1})		Median reflectivity (dBZ)	
	URSWHI	URSWLO	URSWHI	URSWLO	URSWHI	URSWLO	URSWHI	URSWLO
4 Jan 2018	7.2	9.3	180	150	1.26	0.74	16.64	8.36
18 Jan 2020	6.2	8.3	165	150	1.15	0.78	19.95	5.78
16–17 Dec 2020	7.2	8.3	180	180	1.08	0.88	13.00	–3.36
31 Jan–1 Feb 2021	9.3	11.4	165	135	1.29	0.77	7.77	4.32
All cases	7.2	9.3	165	150	1.18	0.79	14.45	4.24

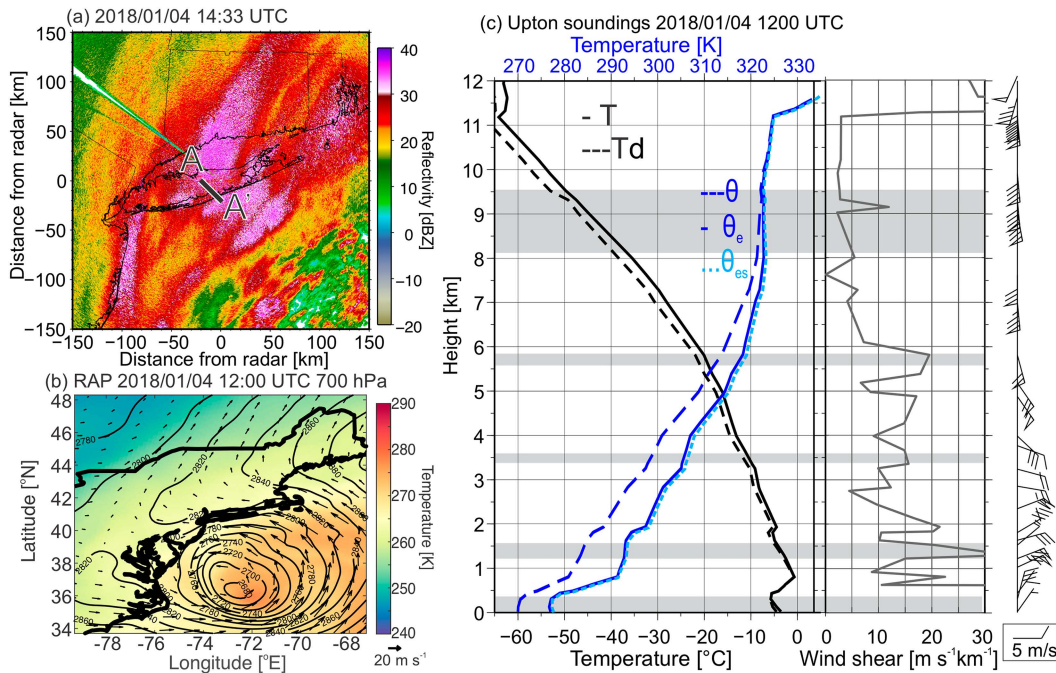


FIG. 6. (a) Horizontal distribution of KOKX reflectivity from a PPI scan at an elevation angle of 0.5° at 1433 UTC 4 Jan 2018. (b) 700-hPa temperature (color shade), geopotential height (contours) and horizontal wind (arrows) from RAP reanalysis data at 1200 UTC 4 Jan 2018. (c) Sounding profiles of temperature (black solid line), dewpoint temperature (black dashed line), potential temperature (θ , blue dashed line), equivalent potential temperature (θ_e , blue solid line), saturated equivalent potential temperature (θ_{es} , light blue dashed line), and vertical wind shear estimated from Eq. (2) (gray line in the right panel) at 1200 UTC from OKX. Gray shaded layers in (c) represent layers of $mRi < 0.25$. The A–A' line in (a) represents the KASPR RHI direction shown in Figs. 7a–c.

4–7 km is collocated with a relatively large SW of approximately 0.4 m s^{-1} in VPT (Fig. 7f). The SW layers presented in the VPT measurements are consistent with the vertical wind shear shown at 5–6 km MSL in the RHI Doppler velocity A–A' (Fig. 7b) and sounding profile (Fig. 6c). They suggest a role of turbulence in forming convection and intensifying snow.

To investigate the spatial characteristics of URs associated with wind shear, we show locations of the detected updraft regions (dots) in the height–time cross section fields for individual cases in Fig. 8a, with color shade representing SW from the KASPR VPT measurements and grayscale representing KASPR reflectivity from VPT. We also show wind directions (color shade) and vertical wind shear (contours) from the KASPR VAD analysis in Fig. 8b. To examine a relation with a large-scale forcing, we also show the time series of frontogenesis at 600, 700, 775, and 800 hPa (Bluestein 1993) using RAP reanalysis data in Fig. 8c. The $mRi < 0.25$ calculated from sounding and KASPR VAD data is shown in Fig. 8d by magenta contours.

URs are more frequently observed during the first snowband period (1110–1800 UTC), suggesting a contribution of URs to the snowbands, as shown in the previous studies. The URs are also observed outside the snowbands. A difference between the URs during the first snowband and those outside the first snowband period is that the URs during the first more accompanied URSWHIs above 2 km MSL (Fig. 8a,

represented by brown–red dots). The URSWHIs appear in the midlevel of the cloud, consistent with the earlier snowband period producing reflectivity $> 20 \text{ dBZ}$ below 4-km altitude, which is 5-dB stronger than that of the latter snowband (Fig. 8a). The URSWHI height is 6 km at 1300 UTC and then descends to 3.5–4 km at 1800 UTC (Fig. 8a). URSWLOs (represented by yellow–green dots) are found at 2 km below the cloud top before the snowband period from 1000 UTC through the entire period of precipitation until 0000 UTC 5 January.

From the KASPR VAD (Fig. 8b), the period (1300–1800 UTC) when URSWHIs dominate the midlevels corresponds to the easterly wind associated with the cyclone below 5 km. This low-level wind produces a vertical wind shear with the upper-level southerly wind shown in the sounding (Fig. 6c). The low-level easterly flow corresponds to the veering wind around the storm center accompanying warm air shown at 700 hPa. The URSWHIs are also collocated with vertical wind shear $> 20 \text{ m s}^{-1} \text{ km}^{-1}$ in the KASPR VAD (Fig. 8b, black contour). This is consistent with the low $mRi < 0.25$ (Fig. 8d, contour) suggesting shear instability. The number of the URs decreases after 1830 UTC close to the end of the first snowband passage and the frontal passage. The low mRi is still present at 4 km altitude, but the wind direction changes to north to northwesterly. The earlier snowband period (1110–1800 UTC) is well associated with 600-hPa frontogenesis, with a peak exceeding $10 \text{ K (100 km)}^{-1} (3 \text{ h})^{-1}$ (Fig. 8c, light blue), while there is

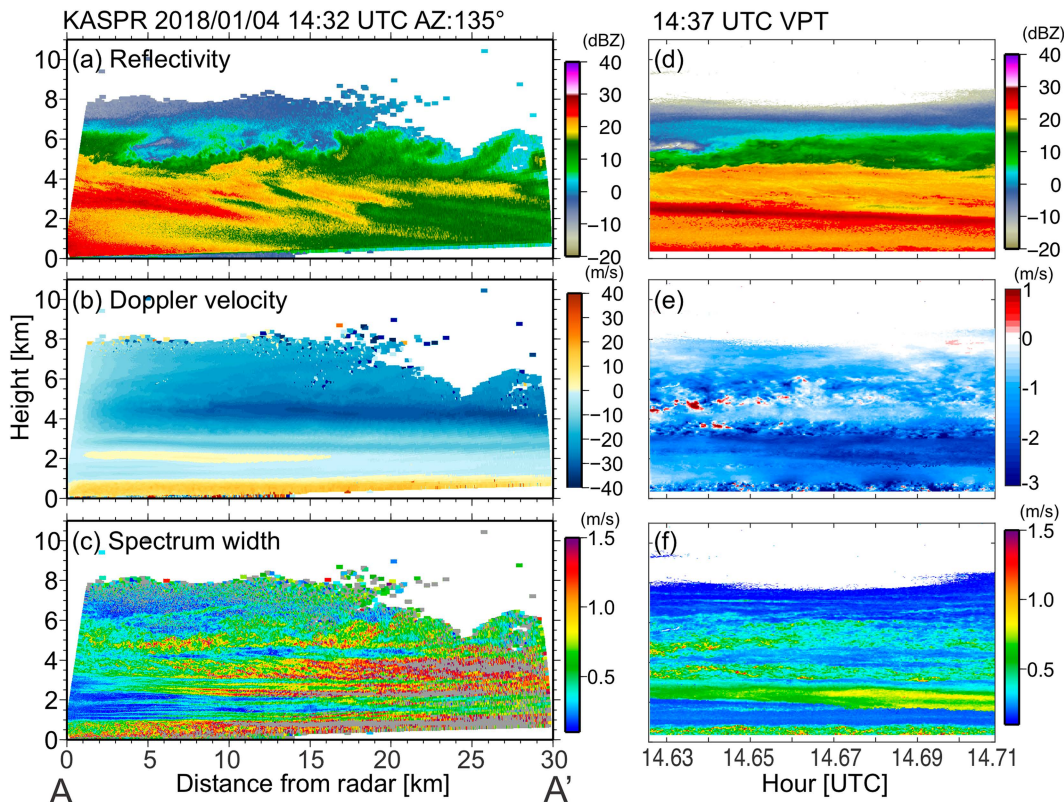


FIG. 7. (left) Vertical cross sections of KASPR (a) reflectivity (shaded; in dBZ), (b) Doppler velocity (in m s^{-1}), (c) Doppler spectrum width (in m s^{-1}) from an RHI scan along A–A' line in Fig. 6a at 1432 UTC and (right) height-vs-cross sections of KASPR (d) reflectivity, (e) Doppler velocity, and (f) Doppler spectrum width from the VPT measurements.

700-hPa frontogenesis exceeding $15 \text{ K} (100 \text{ km})^{-1} (3 \text{ h})^{-1}$ for the latter snowband (1900–2110 UTC; Fig. 8c, blue).

The height–time cross sections of bulk mass flux and the time series of column mean mass flux are displayed in the time series plots in Figs. 8d and 8e, respectively. Figure 8d also shows the mRi less than 0.25. Generally, the URs contributed to upward bulk mass flux when they are clustered in space and time. The URs during the snowbands above 2 km contributed relatively large mass flux (Fig. 8d), and the URSWHIs contribute to slightly larger mass flux compared to URSWLO (Fig. 8e) during the snowband periods, likely due to slightly stronger updrafts (Table 3). For the 4 January case, the latter snowband accompanied less URs producing smaller bulk mass flux and smaller reflectivity (Figs. 8a,e), likely because the URs were not clustered in space in time.

The upward bulk mass flux occurs within and above the moist shear instability ($\text{mRi} < 0.25$) layers (Fig. 8d) and the layers of large vertical wind shear $> 30 \text{ m s}^{-1} \text{ km}^{-1}$ (Fig. 8b, gray contour). This suggests a role of shear instability for generating URs and hence upward mass transport. Those were common features for the three multiband cases (4 January first band, 16–17 December, and 1 February, shown later).

Figure 9a shows the vertical distributions of the URs. The total length of each bar is the accumulated time with updrafts

divided by the accumulated time with cloud echo as a percent at each altitude bin (0.5 km). The UR accounts for more than 10% of cloud-echo time at almost all levels with the maximum of 31% at 5-km altitude. The URs are classified into URSWHI and URSWLO, shown by color-coded subsets along each bar. For this case, URs collocated with $\text{SW} > 0.4 \text{ m s}^{-1}$ (URSWHIs) account for approximately 30% of the total number of URs above the PBL height (Table 2) with the maximum at 5-km altitude. This was common for the three multiband cases.

Figure 9b shows profiles of the occurrences (time relative to the total cloudy time) at each height similar to Fig. 9a, but for wind shear $> 15 \text{ m s}^{-1} \text{ km}^{-1}$ and $\text{mRi} < 0.25$. The midlevel UR and URSWHI are well correlated with wind shear (red line, correlation of 0.76 between URSWHI and wind shear). The wind shear is also correlated with the moist shear instability ($\text{mRi} < 0.25$, correlation of 0.58). Note that the VAD-based wind data are limited to 7.8 km maximum altitude. Sounding in Fig. 6c shows the shear instability ($\text{mRi} < 0.25$) at 8–9.5 km, consistent with local peak of the UR and URSWHI occurrences.

2) 16–17 DECEMBER 2020

At 0200 UTC, surface low pressure ($\sim 1006 \text{ hPa}$) was along the mid-Atlantic coast and moved northward offshore during

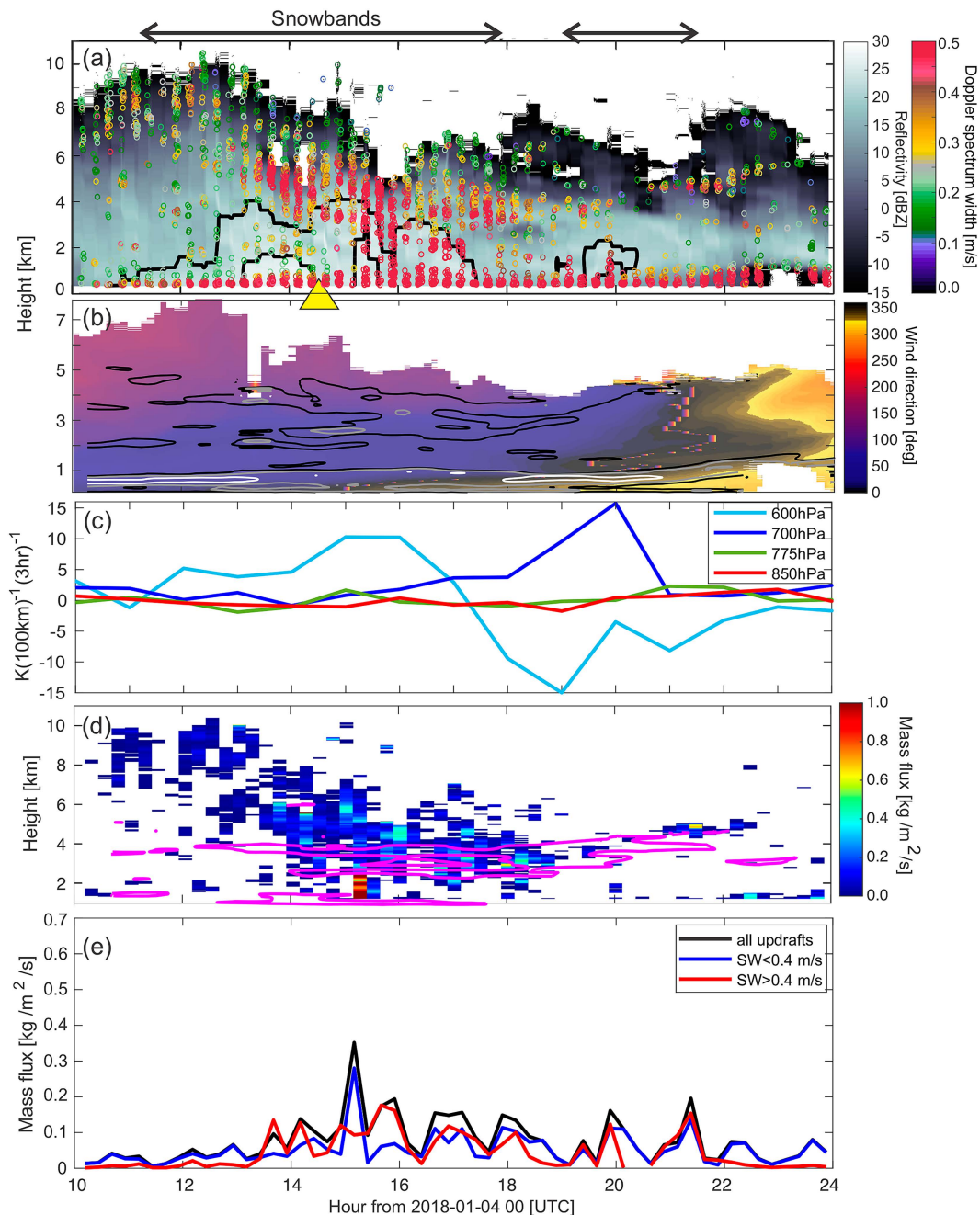


FIG. 8. (a) Height-vs-time cross sections of KASPR reflectivity from VPT (grayscale) and locations of detected updraft regions (color dots) for 4 Jan 2018. Black contours represent KASPR reflectivity > 20 dBZ with 5-dB increment. Horizontal arrows at the top represent the period of snowband passages at SBU. The yellow triangle indicates the time of the snowbands near SBU shown in Fig. 4 and RHI measurements shown in Fig. 7. (b) Height-vs-time cross sections of wind direction (color shade) and vertical wind shear of 0.02 , 0.03 , and 0.05 s^{-1} (black, gray, and white contours, respectively) estimated from KASPR VAD. (c) Time series of frontogenesis at four levels estimated using RAP reanalysis data for 4 Jan 2018. (d) Height-vs-time cross sections of the bulk mass flux (color shade) and mRi smaller than 0.25 (magenta contour). The mass flux is averaged every VPT file at each height. (e) Time series of column mean mass flux estimated from the detected updraft regions averaged over altitude. The mass flux is averaged every VPT file and then averaged over altitude. Black line represents the column mean mass flux from the contributions of all detected updraft regions, and blue and red lines represent that of updraft regions with $\text{SW} < 0.4$ and $> 0.4 \text{ m s}^{-1}$, respectively.

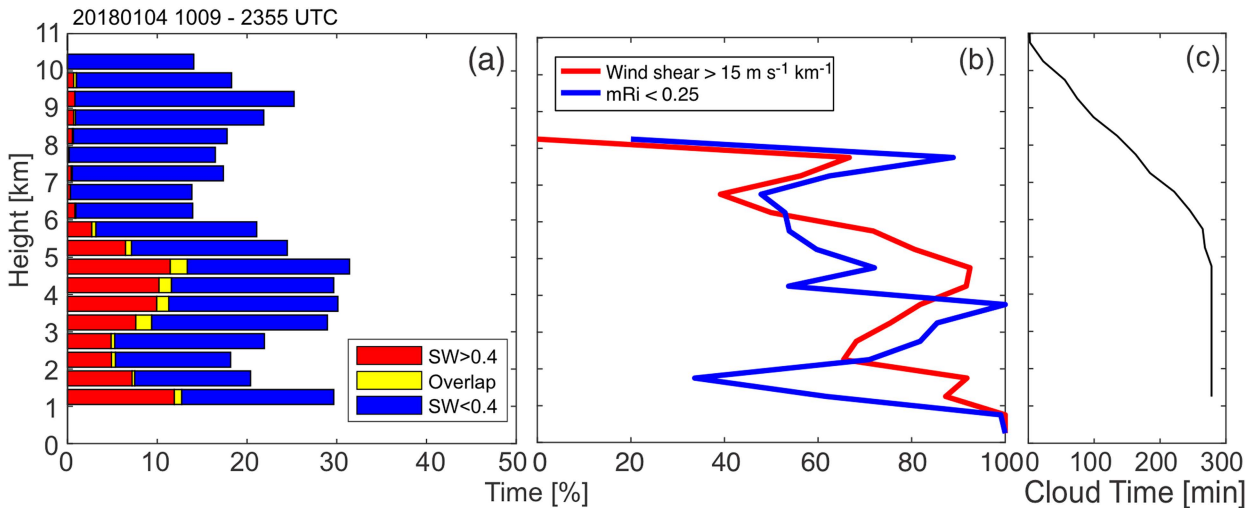


FIG. 9. (a) Histograms of occurrence (time relative to the total cloudy time observed by KASPR VPT) of detected updraft regions shown as percentage of the entire cloud-echo time at each altitude for the cases of 4 Jan 2018. The color bars represent different magnitudes of mean Doppler spectrum width (SW) with a SW threshold (red: SW > 0.4 m s⁻¹; blue: SW < 0.4 m s⁻¹). The SW from the KASPR VPT measurements was averaged over each updraft region. The 15-m vertical resolution data were resampled every 0.5 km height. In a resampled 0.5-km height range, some URs located in different heights can be overlapped in time. Periods where UR having SW > 0.4 m s⁻¹ and UR having SW < 0.4 m s⁻¹ are overlapped in time are represented by yellow bars. (b) Occurrences of wind shear > 15 m s⁻¹ km⁻¹ (red) and mRi < 0.25 (blue) normalized by the entire cloud-echo time at each altitude for the cases of 4 Jan 2018. (c) Profiles of the time used for the analysis at each height bin. The analysis was based on the VPT scans for 5-min duration every 15 min. The total analysis period is also shown in Table 1.

the next 24 h (orange track in Fig. 4). Similar to the 4 January case, Fig. 10 shows the horizontal distributions of the NEXRAD reflectivity at the time of snowbands, 700 hPa RAP, and the 0314 UTC 17 December sounding profile. A well-defined warm

front existed to the north of the surface cyclone stretching from west to east south of Long Island, with warm advection at 700 hPa over Long Island (Fig. 10b). The west-northwest-east-southeast-oriented snowbands exceeding 30 dBZ passed over SBU from

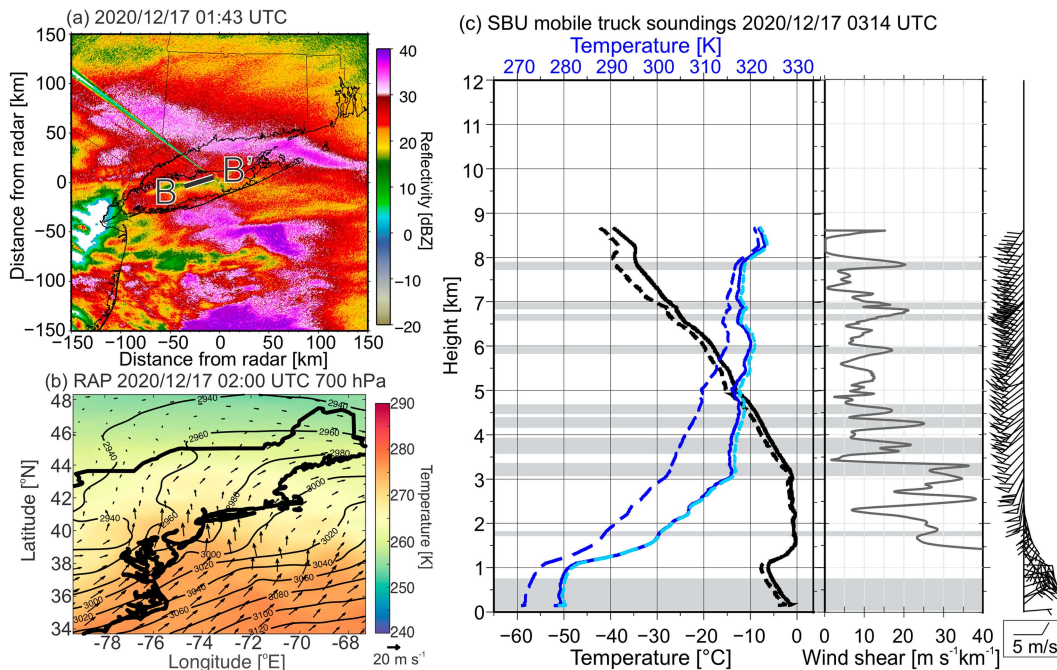


FIG. 10. As in Fig. 6, but at (a) 0143, (b) 0200, and (c) 0314 UTC 17 Dec 2020 collected at Stony Brook (green triangle in Fig. 1). The B–B' line in (a) represents the KASPR RHI direction shown in Figs. 11a–c.

south to north from 0000 to 0310 UTC 17 December (Fig. 10a). The SBU surface temperature was below freezing until 0900 UTC 17 December, while soundings at 0000, 0606, and 0715 UTC 17 December at SBU show an inversion layer and a temperature $> 0^{\circ}\text{C}$ centered around 1.5, 2.3, and 2.4 km MSL, respectively. KASPR RHI observed a melting layer after 0350 UTC 17 December at 2.5 km MSL. We focus on the period prior to the melting signature (Table 1).

Figure 11 shows the KASPR RHI and VPT scans near a snowband at around 0130 UTC 17 December. The KASPR RHI scans (Figs. 11a–c) reveal generating cells at cloud top, with areas of relatively large SW ($>0.75\text{ m s}^{-1}$) from 6 to 7.5 km MSL, and fallstreaks extending downward to the west below 6 km MSL where their directions are modified by the wind shear at around 5.4 km MSL (Figs. 10c and 11b). The KASPR VPT measurements (Figs. 11d–f) also reveal updrafts with large SW ($>0.4\text{ m s}^{-1}$) in the generating cell layer. The cloud-top generating cells are in conditionally unstable layers with smaller regions of moist absolutely unstable layer (MAUL; Bryan and Fritsch 2000) as $\partial\theta_e/\partial z < 0$ and $\partial\theta_{es}/\partial z < 0$ with $\theta_e \approx \theta_{es}$ at 6–6.5 and 6.8–7.0 km MSL (Fig. 10c). These layers correspond to the vertical wind shear layer observed by the RHI (Fig. 11b). The sounding had several layers of vertical wind shear layers ($>20\text{ m s}^{-1}\text{ km}^{-1}$), most of which above 3 km MSL were linked to shear instability ($\text{mRi} < 0.25$).

Figure 12 depicts the time series of the spatial distributions of URs, horizontal wind, frontogenesis, mRi, and mass flux for the case of 16–17 December 2020, similar to Fig. 8. The snowband period is also closely associated with the 600-hPa frontogenesis, with the peak exceeding $15\text{ K (100 km)}^{-1}$ ($3\text{ h})^{-1}$ at 0200 UTC 17 December (Figs. 12a,c). While the URs are observed throughout the event, during the snowband period URs dominate in the cloud depth above 2 km. URSWLOs are found within 2 km from the cloud-top height starting before the snowband period from 1930 UTC 16 December to 0200 UTC 17 December (Fig. 12a). URSWHIs appear from 2100 UTC 16 December just below the URSWLO layer, corresponding to the period that includes larger reflectivity $> 25\text{ dBZ}$ below 2 km (2230–0010 UTC) and below 4.5 km (0030–0145 UTC, snowband period). During the snowband period, URSWHIs are more prominent in a deeper layer between 4 km to the cloud top. The KASPR VAD analysis (Fig. 12b) shows that the lower boundary of the URSWHI layer well corresponds to vertical wind shear $> 20\text{ m s}^{-1}\text{ km}^{-1}$ (Fig. 12b) starting at 6.2 km altitude at 2100 UTC until 3–4 km at 0230 UTC and low $\text{mRi} < 0.25$ (Fig. 12d, contour).

In the occurrence profile in Fig. 13, similar to the 4 January case, the UR accounts for more than 10% of cloud-echo time at almost all levels. The maximum occurrence of URs is found at 9 km, but the maximum occurrence of URSWHIs is found at lower altitude around 6.5 km. The occurrence profile of the wind shear in Fig. 13b is somewhat noisy, but the shear of the wind direction (green line) is consistent with URSWHIs (black line, correlation of 0.33).

Similar to the 4 January case, the upward bulk mass flux occurs within the moist shear instability ($\text{mRi} < 0.25$) layers (Fig. 12d). This suggests a role of shear instability for generating URs and hence upward mass transport. The mass flux

shows a maximum during the snowband period where the URSWHIs are clustered, suggesting a contribution of URSWHIs to the upward mass transport.

3) 1 FEBRUARY 2021

Similar to 16–17 December, the snow event was associated with a surface cyclone moving northward to the south of Long Island (green track in Fig. 4). No snowbands were evident around Long Island before 0210 UTC 1 February. After 0210 UTC 1 February, there were precipitation areas with reflectivity $> 30\text{ dBZ}$ around SBU, but they were not banded until 1300 UTC 1 February. From 1400 to 1830 UTC 1 February, two west–east-oriented snowbands (30–40 dBZ) crossed SBU moving northward (Fig. 14). As shown in Fig. 14b, there was a surface warm front just south of Long Island, with warm advection at 700 hPa over this region.

Figure 14c shows the SBU sounding at 1843 UTC 1 February near the snowband period. The sounding profile shows that a moist unstable layer exists near cloud top (4–5.2 km MSL). The KASPR RHI measurements in Fig. 15 reveal cloud-top generating cells at 5.2–7.5 km MSL near the moist unstable layer and fallstreaks to 25 dBZ underneath the generating cell layer during the snowband period (Figs. 15a,d). The Z difference between the WSR-88D and KASPR likely represents a resonance scattering effect at Ka band owing to the presence of larger snow particles relative to the wavelength. The sounding for the generating cell layer includes moist instability, and wind shear instability ($\text{mRi} < 0.25$; Fig. 14c). This layer also corresponds to supersaturation with respect to ice (not shown). The VPT measurements shown in Figs. 15d–f show updrafts and large SW, indicating that the generating cells accompanied turbulence. The cloud-top generating cell layer is also well consistent with the Doppler velocity shear (Fig. 15b). Interestingly, there is also a layer of updrafts collocated with relatively large SW ($>0.4\text{ m s}^{-1}$; Figs. 15e,f) at 2 km in the VPT, well consistent with vertical wind shear observed by the RHI (Fig. 15b) and the sounding measurements (at 2.5 km; Fig. 14c).

As shown in the time series of this case shown in Fig. 16, the snowband period is associated with a 700-hPa frontogenesis of 7 K (100 km)^{-1} ($3\text{ h})^{-1}$ at 1800 UTC, and the 775-hPa frontogenesis maximum of $15\text{ K (100 km)}^{-1}$ ($3\text{ h})^{-1}$ at 2000 UTC (Figs. 16a,c). URSWLOs (represented by yellow–green dots) are observed near the cloud top with weak reflectivity ($< \sim 0\text{ dBZ}$) from the beginning of the observation on 31 January (1800 UTC) until 1300 UTC 1 February. URSWHIs occur from 1200 UTC 1 February to the end of the analysis period (0000 UTC 2 February), which is consistent with the snowband period. The KASPR VAD analysis (Fig. 16b) shows the vertical wind shear produced by south-southeasterly wind in the low altitudes and southwesterly wind in the upper altitudes. The shear line is found between 2- and 3-km altitudes until 1210 UTC 1 February and then ascends to 6-km altitude by 1400 UTC. The low-level south-southeasterly wind corresponds to the 700-hPa warm advection presented in the RAP data at 1400 UTC (Fig. 14b).

In the occurrence profile in Fig. 17, similar to the other multiband cases, the UR accounts for more than 10% of cloud-

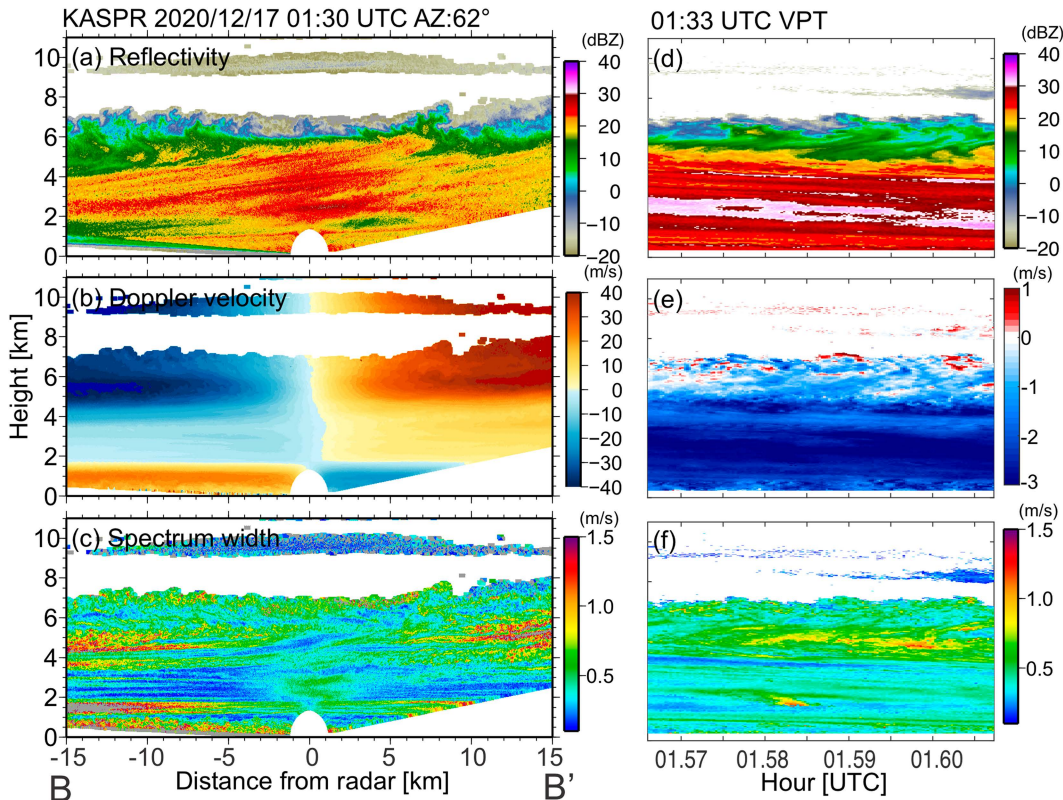


FIG. 11. As in Fig. 7, but (a)–(c) at the 0130 UTC RHI scan along B–B' line in Fig. 10a on 17 Dec 2020 and (d)–(f) VPT measurements on 17 Dec 2020.

echo time at almost all levels with the maximum of UR (and URSWLO) occurrence is found near the cloud top. The maximum occurrence of URSWHIs is found at lower altitude around 7 km, and the second peak is found at around 3 km. These peaks in the URSWHI occurrence are well consistent with the peaks of the occurrence of large wind shear (red line, correlation of 0.24 with URSWHI). The URSWHI occurrence is also well correlated with low mRi (correlation of 0.63).

4) 18 JANUARY 2020

For the 18 January case, which accompanied a single snowband, by 0300 UTC 19 January, the surface warm front associated with a surface cyclone (~ 1003 hPa) centered over northern Michigan was southwest of Long Island along the mid-Atlantic coast as the storm center moved eastward (magenta track in Fig. 4). The vertical wind shear seemed similar to the multi-band cases, but the spatial distributions of UR and the radar reflectivity showed some differences. Figure 18 shows the horizontal distributions of the NEXRAD reflectivity at the time of snowbands, 700 hPa RAP, and the 1813 UTC sounding profile. The warm-frontal snowband (>20 dBZ) oriented from northwest to southeast crossed SBU between 1830 and 2015 UTC 18 January (Fig. 18a) accompanying a 700-hPa warm advection (Fig. 18b). The maximum WSR-88D reflectivity for this snowband (~ 30 dBZ) was 5–10 dB weaker than the other cases. The surface precipitation transitioned to rain after the warm frontal

snowband passage. This study focuses on the warm frontal snowband to avoid uncertain errors associated with hydrometeor attenuation in the rain layer.

The sounding from the SBU mobile truck deployed at Cedar Beach (blue triangle of Fig. 1) at 1813 UTC 18 January, which was closest to the snowband passage, shows a warm-frontal stable layer with veering winds from 1 to 2 km MSL and a near moist neutral layer from 2 to 3 km MSL (Fig. 18c). The sounding in Fig. 18c and KASPR measurements in Fig. 19 suggest that the cloud-top height reach 10 km MSL, where the vertical profile is less stable and near moist neutral (7–10 km MSL). KASPR RHI scans oriented northeast–southwest (B–B' in Fig. 18a) and crossing the snowband (Figs. 19a–c) reveal a gradual increase of reflectivity toward the surface above ~ 3 km MSL and relatively uniform reflectivity at a given altitude when the snowband passed. The VPT measurements (Figs. 19d–f) do not show significant convection above 4 km, where the RHI Doppler velocity shows less vertical wind shear. There is a wave-like feature at the radar echo top (at ~ 10 km; Figs. 19a–c) with weak reflectivity, which could be a source of precipitation. The VPT measurements show layers of relatively large SW at 2 and 4 km. These layers also correspond to the vertical wind shear observed by the RHI and shear unstable layers observed by the sounding ($mRi < 0.25$, gray shades). The lower layer (2 km MSL) corresponds to a local intensification of reflectivity (~ 25 dB). These SW values, however, weaker (generally <0.4 m s $^{-1}$) than the other cases (Fig. 19f).

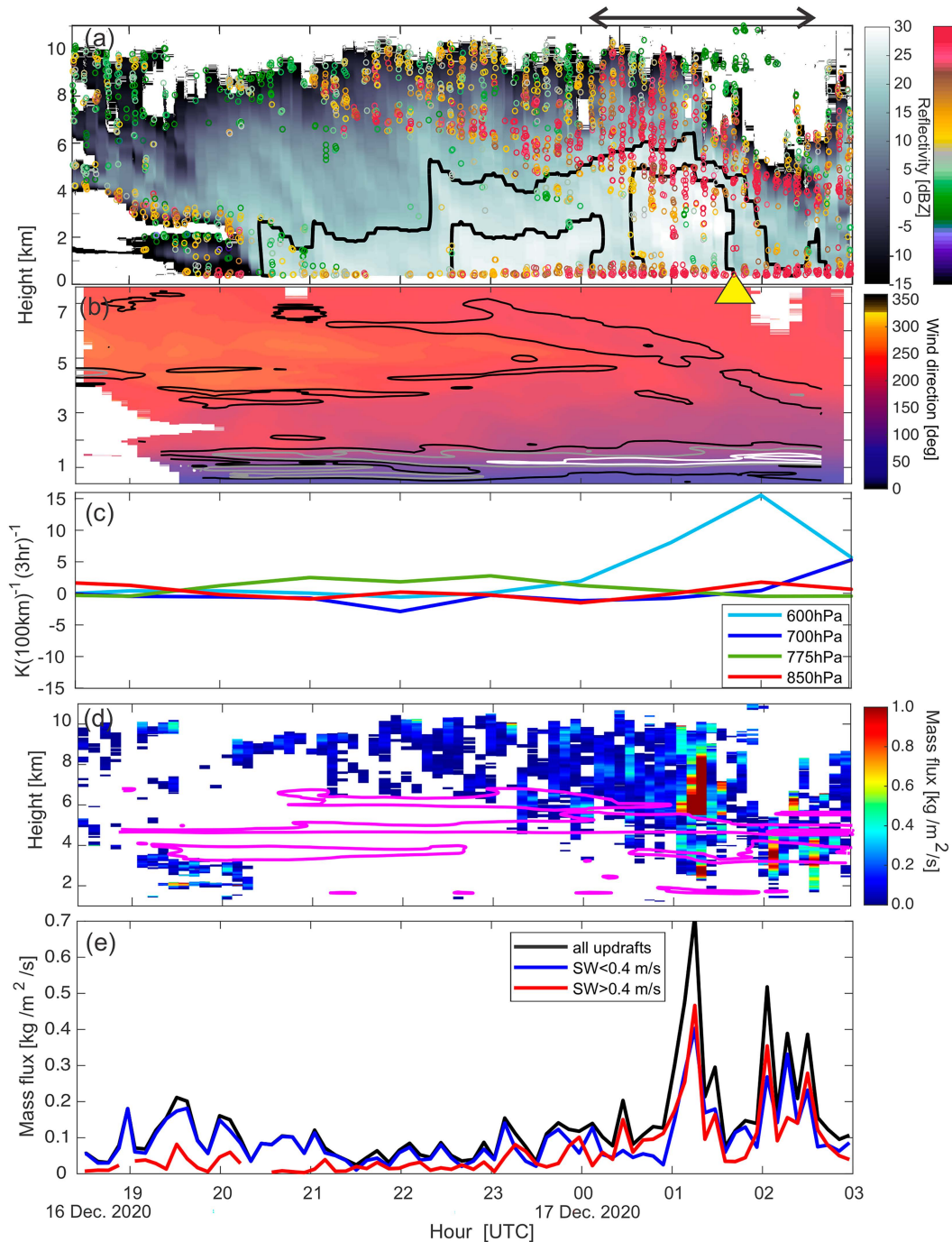


FIG. 12. As in Fig. 8, but for 16–17 Dec 2020.

Figure 20 shows the set of time series for the 18 January case. Similar to the other three cases, URSWLOs (represented by yellow–green–blue dots) are observed near the cloud top with weak reflectivity (< 0 dBZ), but the frontogenesis was very weak at all levels [< 2 $\text{K} (100 \text{ km})^{-1} (3 \text{ h})^{-1}$ at 700, 775, and 800 hPa; Fig. 20c]. Multiple layers of vertical wind shear $> 30 \text{ m s}^{-1} \text{ km}^{-1}$ (Fig. 20b) are observed within

the cloud, similar to the other three cases. In contrast to the three multiband cases, for the 18 January case, no significant increase in the mass flux is found (Figs. 20d,e). Near the cloud top, where URSWLOs dominate, the mass flux varies in magnitude and is discontinuous in time.

Figure 21 shows the occurrence profiles. The UR accounts for less than or equal to 10% of cloud-echo time at 2.5 km,

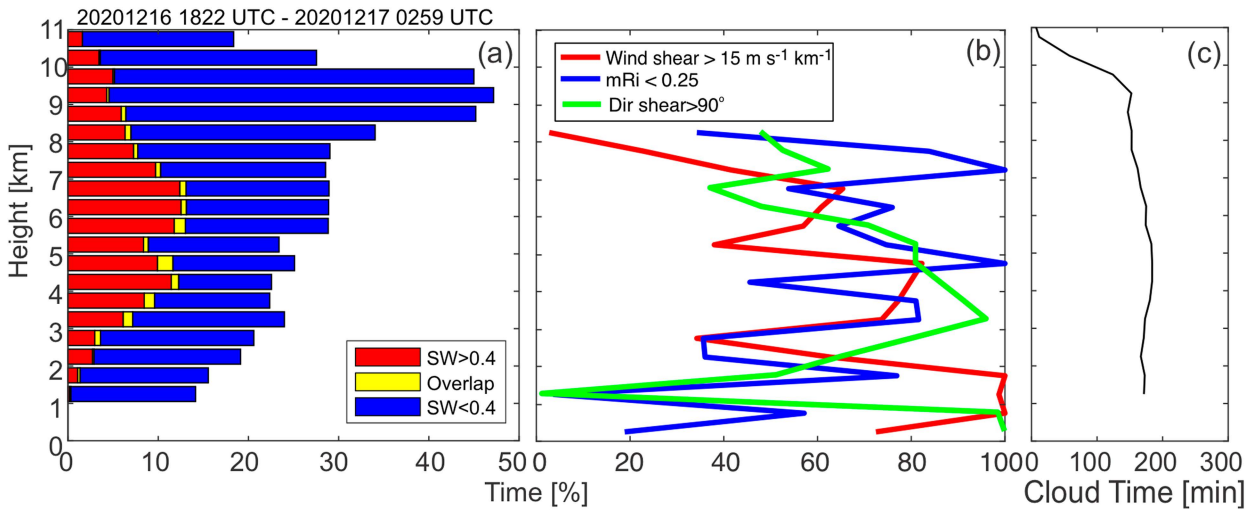


FIG. 13. As in Fig. 9, but for 16–17 Dec 2020. The occurrence of direction shear of horizontal wind $> 90^\circ \text{ km}^{-1}$ is also shown in (b) by a green line.

and URSWHI accounts for only 3% at all levels (Fig. 21a). Although the number of URSWHIs is small, the occurrences of UR and URSWHI are correlated with the large wind shear (red line, correlation of 0.48 with URSWHI; Fig. 21b). They are also weakly correlated with shear instability; the correlation between UR (gray line) and low mRi (blue line) is 0.30, and that between large wind shear (red line) and low mRi (blue line) is 0.57. While the layers of updraft regions and wind shear were correlated, the strength of wind shear or

shear instability might not be a factor of the strength and frequency of the updrafts. Further analysis is needed to evaluate this using high-resolution model simulations.

c. Summary

The snowbands accompanied convective cells near cloud top and fallstreaks underneath, as observed by the previous studies. The convective cells were well collocated with layers of updrafts and large SW associated with vertical wind shear.

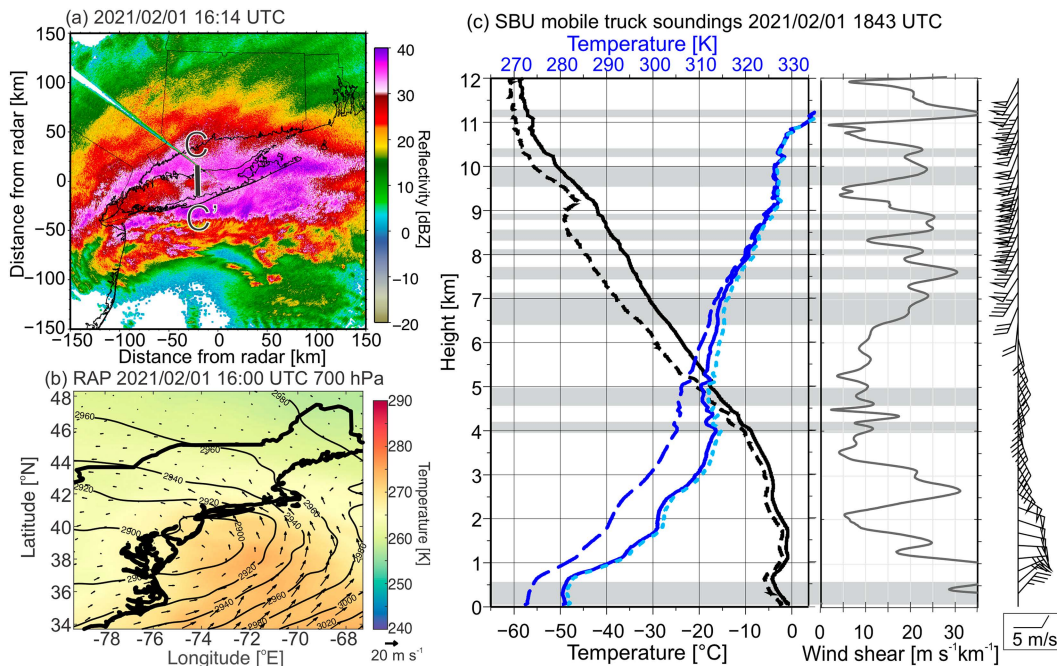


FIG. 14. As in Fig. 6, but at (a) 1614, (b) at 1600, and (c) 1843 UTC 1 Feb 2021 collected at Stony Brook (green triangle in Fig. 1). The C-C' line in (a) represents the KASPR RHI direction shown in Figs. 15a–c.

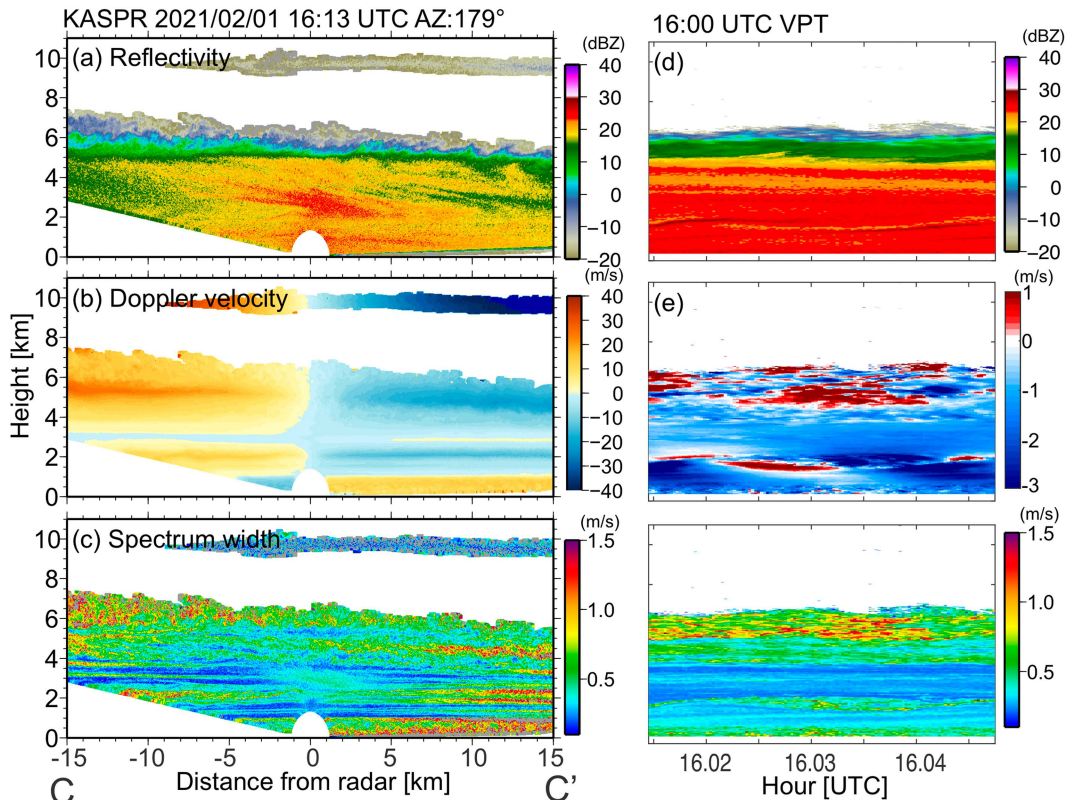


FIG. 15. As in Fig. 7, but (a)–(c) at 1613 UTC RHIs along C–C' line in Fig. 14a on 1 Feb 2021 and (d)–(f) VPT measurements on 1 Feb 2021.

They suggest that the near cloud-top convective cells (i.e., generating cells) contributed to the precipitation within the snowbands. The weak snowband case (18 January) did not show significant updrafts and turbulence (large SW) near the cloud top even within the cloud layer. The URs associated with wind shear were often multilayered in the precipitating clouds, as they were observed not only near the cloud top but also the middle of the precipitating clouds. They were collocated with intensification of the precipitation underneath as measured by reflectivity.

Although there is a case-to-case variability in the heights, the URs collocated with $SW > 0.4 \text{ m s}^{-1}$ (URSWHIs) occur in more interior clouds of the multiband cases. URSWHIs tend to be shorter lived compared to the URSWLOs for all cases (approximately 1–2 s shorter, Table 3). URSWHIs have slightly ($0.20\text{--}0.52 \text{ m s}^{-1}$) stronger median upward motion and 3.5–16.4 dB larger median reflectivity (Table 3). In contrast, URs collocated with $SW < 0.4 \text{ m s}^{-1}$ (URSWLOs) show higher frequencies at higher altitudes. They are found above 8-km altitude; some of them are found very close to the echo tops, and most of them are found within 1–2-km distance from the echo tops. The lower SW is likely due to a combination of less turbulence and a narrower particle size distribution owing to weaker reflectivity. The peak of the URSWHI occurrence is found at a lower altitude than that of the URSWLOs.

Overall, URs are found throughout the snowstorms regardless of the snowband periods or frontogenesis for the four

cases. The occurrences of URs and URSWHIs are well correlated with large wind shear and shear instability (Figs. 9, 13, 17, and 21). The URSWHIs are frequently found during the snowband periods for three of the cases.

4. Discussion

Novel high-vertical-resolution, high-sensitivity vertically pointing radar measurements in four winter storms along the U.S. northeast coast showed that URs are ubiquitous features in the winter storms. They are correlated with layers of enhanced wind shear and are found frequently in the presence of snowbands, which suggests that URs could promote precipitating particle growth. They accompanied the snowbands, but they also occurred outside the snowbands. This suggests that the URs could promote precipitating particle growth. In particular, high-reflectivity bands from 4 January, 16–17 December, and 1 February accompanied URSWHIs. They suggest that URs associated with the wind shear contributed to the formation and/or intensification of snowbands. This is consistent with previous studies (e.g., Plummer et al. 2014; Rauber et al. 2014). The present study revealed that the URs contributed to particularly significant upward mass flux when they were clustered in space and time especially during the snowband periods. RAP 700-hPa specific humidity $> 5 \text{ g kg}^{-1}$ (not shown) was associated with periods with the larger mass flux in all four cases. It

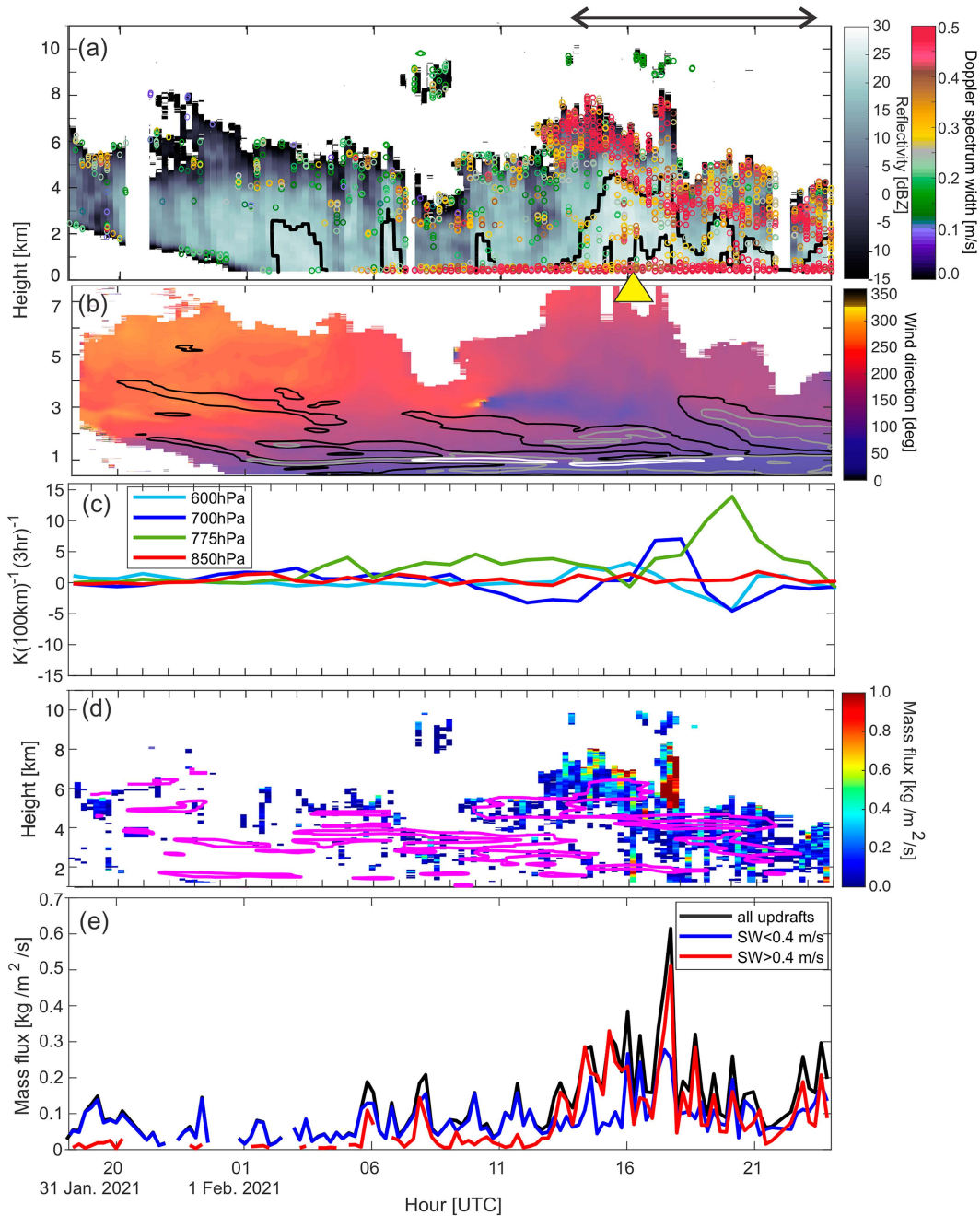


FIG. 16. As in Fig. 8, but for 31 Jan–1 Feb 2020.

is suggested that the URs could play a role as a driver for supplying water vapor that could produce saturation with respect to liquid water and thus potentially the formation of supercooled liquid droplets. They could then contribute to forming/growing precipitation particles, as pointed out by Plummer et al. (2014). The URs were observed not only in the snowbands, but also outside the snowbands, although they were distributed sparsely compared to within the snowbands. This suggests a role of the URs on snow particle formation and/or intensification of snowfall outside the snowbands.

The URs, especially URSWHIs were well correlated with vertical wind shear and shear instability ($mRi < 0.25$; Figs. 8, 9, 12, 13, 16, 17, 20, and 21), suggesting that vertical wind shear caused turbulence, which included upward vertical velocity perturbations identified here as URs. The large mass flux is particularly associated with the moist shear instability, suggesting a role of the turbulence induced URs on the vertical mass transport. The wind shears were multilayered in the cloud systems. This is consistent with former studies such as Boucher et al. (1965), Wexler et al. (1967), Syrett et al. (1995),

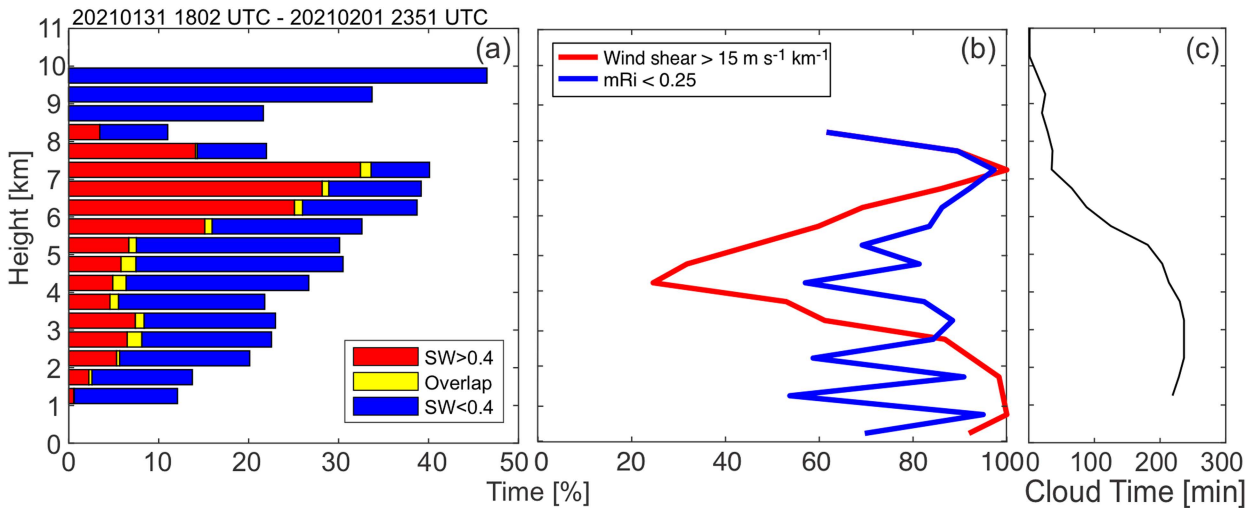


FIG. 17. As in Fig. 9, but for the case of 1 Feb 2021.

and Rauber et al. (2014) that observed wind shears associated with frontal zones in winter storms using Doppler radar measurements. This suggests that the snowstorm systems in the present study were composed of several air masses originating from different sources producing frontal zones, as commonly observed by previous studies (e.g., Boucher et al. 1965; Rauber et al. 2014). The KASPR measurements presented in this study also showed wind shear layers with low mRi outside the frontal zones. The multilayers of turbulence and updrafts associated with wind shear observed by the RHIs and soundings in

this study suggest the presence of smaller-scale air masses rather than synoptic-scale air masses as presented in Rauber et al. (2014).

It is hard to determine the role of frontogenesis in the UR formation, because frontogenesis, larger-scale (synoptic scale) forcing, associates larger-scale ascending that generally has smaller (cm s^{-1})-scale vertical air motion. The URs and updrafts observed by the vertically pointing radar measurements in this study are finer scales having ~ 10 -s duration and $>1 \text{ m s}^{-1}$ upward velocity than those associated with frontogenesis.

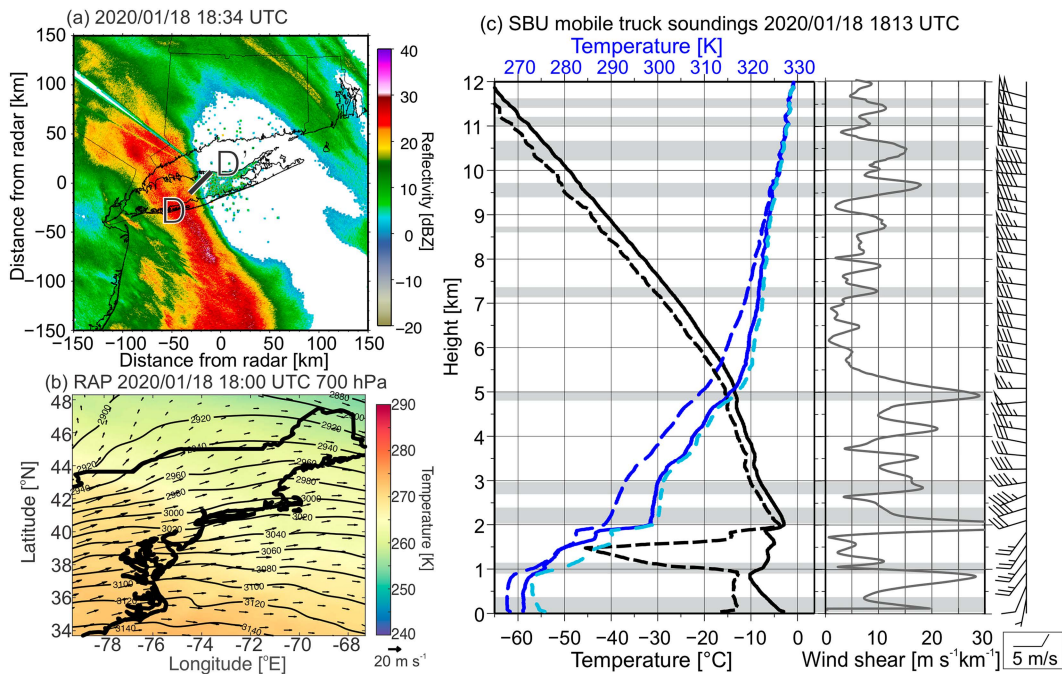


FIG. 18. As in Fig. 6, but at (a) 1834, (b) 1800, and (c) 1813 UTC 18 Jan 2020 collected at Cedar Beach (blue triangle in Fig. 1). The D-D' line in (a) represents the KASPR RHI direction shown in Figs. 19a-c.

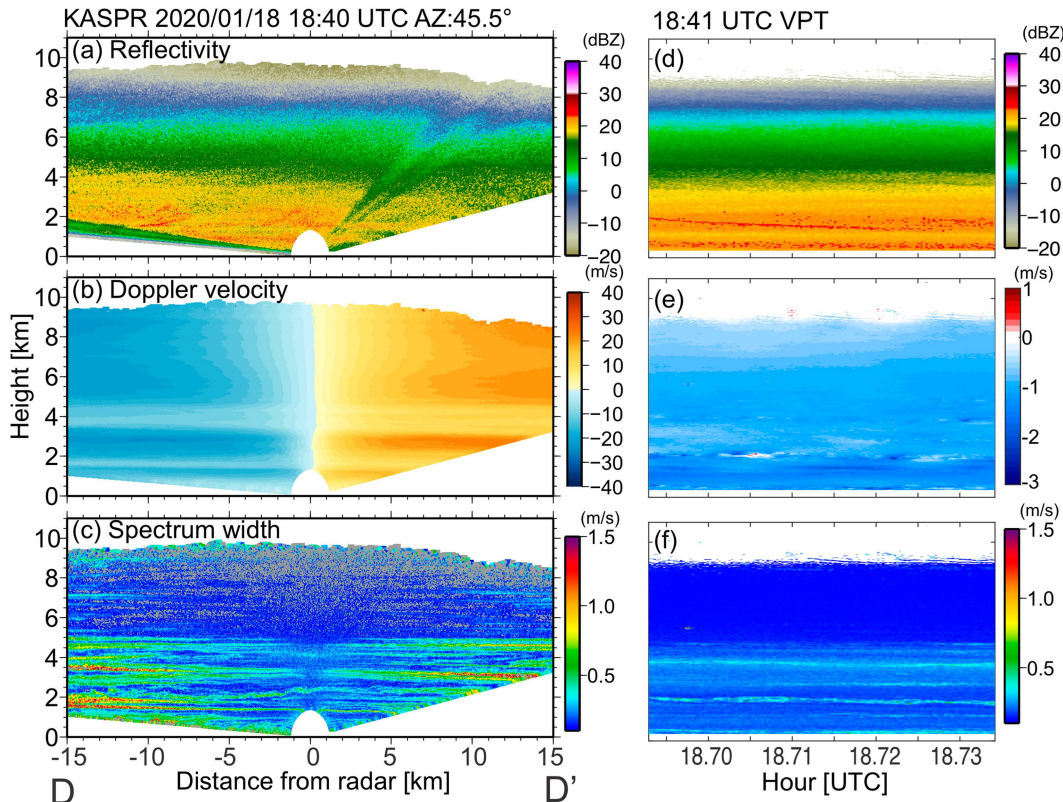


FIG. 19. As in Fig. 9, but (a)–(c) at the 1840 UTC RHI scan along D–D' line in Fig. 18a on 18 Jan 2020 and (d)–(f) VPT measurements on 18 Jan 2020.

It is possible that the updrafts at the cloud tops could be produced in part by instabilities caused by cloud-top radiative cooling. The cloud-top cooling could produce cloud-top destabilization leading to development of generating cells (e.g., Syrett et al. 1995; Keeler et al. 2016a,b). That cooling might pair with heating associated with snow particle growth (depositional and riming growth) within the cloud, resulting in lapse rate maintaining convection (Kumjian et al. 2014). Alternatively, if there was advection of drier and/or cooler (i.e., lower θ_e) air aloft, it could play a role in producing the potential instability, as shown in the soundings from the 16–17 December and 1 February cases. Future studies should examine the relative roles of microscale updrafts as compared to mesoscale and synoptic-scale updrafts.

The wind shear instability (i.e., Kelvin–Helmholtz instability) can also produce downdrafts, which are not focused on in this study. The updrafts can contribute to supplying water vapor producing water saturation and supercooled water in the cells and hence enhancement of particle growth and snow intensification (Plummer et al. 2014; Kumjian et al. 2014), while the downdrafts can play a role in entrainment and sublimation (Raubert et al. 2014). The downdraft regions in this study were found between URs at midlevels and near the cloud tops (e.g., Figs. 11 and 15). The spatial distribution of the downdraft regions was very similar to that of URs, except near the cloud tops. This suggests that URs existed as a UR and downdraft region in the midlevels of the storms. The midlevels of the storms could be

supersaturated, in which case, precipitation particles would not have a chance of much sublimation within the downdraft regions. Near the cloud tops, detecting downdraft regions by the radar measurements might be difficult because hydrometeor particles could be sublimated. Considering the microphysics within the updraft/downdraft regions near the cloud tops and at midlevels should be important to analyze mass/water budgets and entrainment and understand the water cycle within the cloud systems. We will need lidar measurements to observe the clear-air updrafts and downdrafts and high-resolution simulations that resolve the microscale updrafts and downdrafts.

Limited cases in this study (four cases) result in some uncertainty in the relationships between URs and wind shear. Analysis including more cases using the high-resolution radar observations can help to better understand the formation mechanisms of URs and the roles of URs in microphysical processes in winter storms. Model simulations will help to further understand the mechanisms of UR generations and the microphysical impacts, including the sources of multilayers that generate turbulence and ice particle formation, if the models can resolve the wind shear layers and use optimal turbulence kinematic energy parameterization. The model simulations are beyond the scope of this observational study.

The methodology to identify microscale updrafts described in this paper can be applied to other vertically pointing Doppler radar datasets to examine the small-scale velocity structures

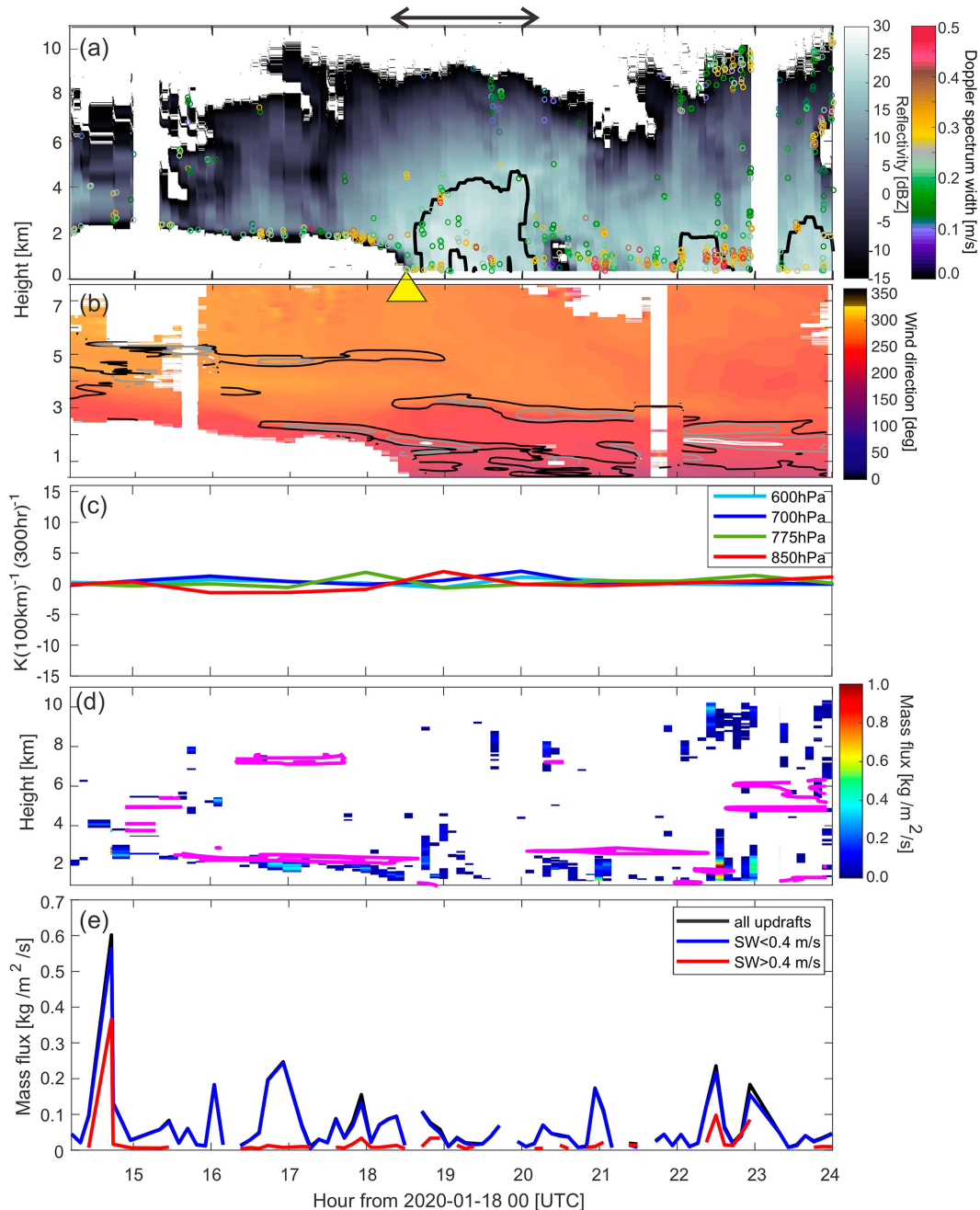


FIG. 20. As in Fig. 8, but for 18 Jan 2020.

that are too fine scale to be resolved by other sensors such as the U.S. National Weather Service PPI scanning radars. Further analysis of microscale updrafts and downdrafts can also shed light on the degree to which ice precipitation mass changes in a more episodic mode (smaller time and space scales) versus a more continuous mode (longer time and scale scales) in winter storms and in stratiform regions. The spatial and time scales of the updrafts in this study are larger than the radar sampling volume (~ 15 m in height and ~ 1 s in time). There can be smaller-scale turbulence

(i.e., eddies) within the sampling volume, which can be observed by higher-resolution radars/lidars (having a few-centimeter-scale resolution; Schmidt et al. 2012; Cooper and Chattopadhyay 2014).

5. Summary

Although microscale upward motions in the snowstorms could play an important role in snow precipitation, their characteristics relative to the snowbands and relationship with vertical wind

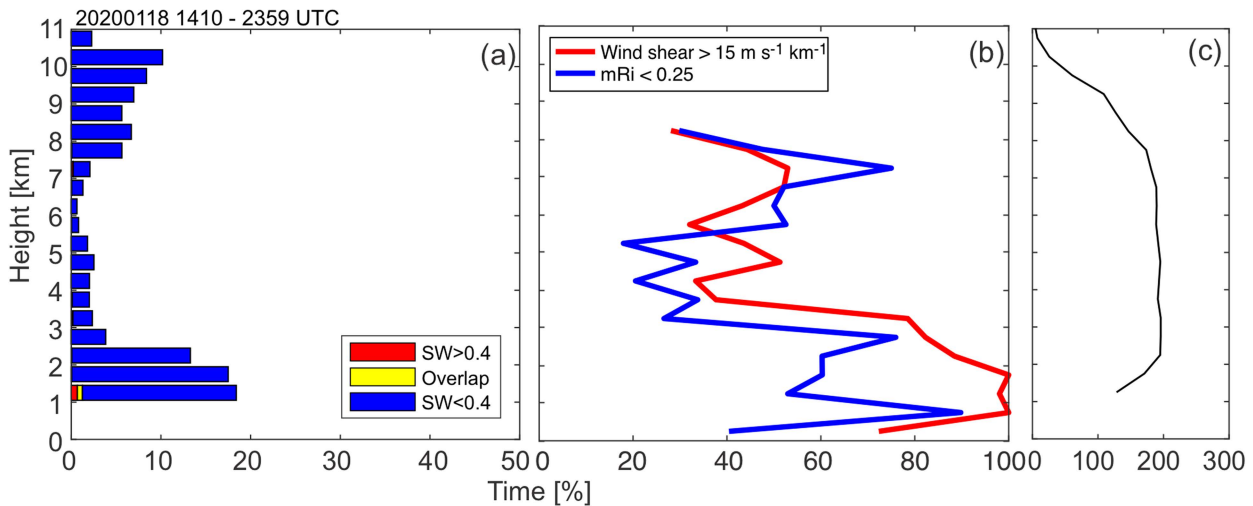


FIG. 21. As in Fig. 9, but for the case of 18 Jan 2020.

shear instability from Kelvin–Helmholtz instability has not been shown yet. We investigated the relations among microscale URs and snowbands, vertical wind shear, shear instability, and frontogenesis, and roles on vertical mass transport for four winter snowstorm cases (4 January 2018, 18 January 2020, 16–17 December 2020, and 1 February 2021). Measurements were made as each storm passed over the SBRO in Stony Brook, New York, and included periods with and without snowbands and in the northwest and northeast quadrants of the three storms (4 January, 16–17 December, and 1 February) and the southwest quadrant of the 18 January storm. Three of the cases (4 January, 16–17 December, and 1 February) included more than one snowband.

The Doppler velocity from the vertically pointing Ka-band polarimetric radar measurements was used to identify updraft regions in this study. After the removal of hydrometeor sedimentation from the VPT measured Doppler velocity, the updraft region was simply defined as a region with the estimated vertical air motion (VPT measured Doppler velocity minus estimated particle fall speed) greater than or equal to 0.4 m s^{-1} (negative sign of Doppler velocity indicates a downward motion). Using vertically pointing radar data does not provide information on the life cycle of the updrafts, but the duration of the updraft overhead can be converted to an estimated spatial scale using horizontal wind estimated from a KASPR PPI VAD technique. We estimated mass flux based on the detected updraft regions and sounding data and investigated relationships among updraft regions, mass flux, and frontogenesis, and shear instability to discuss roles of mesoscale instability on generating the updrafts and vertical mass transport. We summarize the characteristics of the updraft regions and their associations with spectral width, wind shear, and frontogenesis:

- In the vertical pointing radar data, the distribution of updraft durations is approximately logarithmic with most individual updrafts passing overhead in only a few seconds ($<20 \text{ s}$; Fig. 5a). They are roughly equivalent to spatial scales $< 500 \text{ m}$. The aspect ratio of the updraft regions estimated from the duration and horizontal scale has a

lognormal frequency distribution with a modal value near 1 (equivalent to circular; Fig. 5b).

- Overall, snowbands occur in a region of low- to midlevel frontogenesis, but the microscale updraft regions are found at all altitudes, occur both in regions with and without snowbands (Figs. 8a, 12a, 16a, and 20a). They suggest a role of the microscale updraft regions on snow particle formation/or intensification of snowfall not only in the snowbands but also outside the snowbands.
- The subset of updraft regions with larger VPT Doppler spectrum width ($\text{SW} > 0.4 \text{ m s}^{-1}$), which imply more turbulent updrafts, frequently occur within midlevels of the storms (several km below cloud-echo top). They are associated with vertical wind shear and moist shear instability that are sometimes multilayered in the precipitating clouds. They suggest that the updraft regions can be triggered in the shear unstable layers (Figs. 9, 13, 17, and 21).
- Updraft regions that tend to be closer together in space and time yield more bulk mass flux. The duration of individual updraft regions is not the primary factor of the mass flux (Figs. 8e, 12e, 16e, and 20e).
- The calculated upward bulk mass flux occurs within and above the moist shear insurability layers. The highest column mean mass flux is produced during snowband periods (Figs. 8d, 12d, and 16d).

The analysis implies that the dominant forcing of the microscale updrafts appears to be associated with vertical shear instability. The updrafts are responsible for upward mass flux and then contribute to the precipitation mass growth regardless of whether snowbands are present or not. We also detected many microscale updrafts in the boundary layer during portions of each of the four storms but did not focus on them in this study. These low-level updrafts may further modify the microphysics and would be an interesting topic for future studies. Future studies with increasing cases should examine the relative roles of microscale updrafts, downdrafts, and turbulence as compared to mesoscale and synoptic-scale updrafts

and quantitatively estimate the contributions to the mass growth to better understand the precipitation production in winter storms, which in turn may aid in reducing uncertainties in snowfall accumulation forecasts.

Acknowledgments. This work was supported by the National Science Foundation (Yuter: AGS-1347491 and AGS-1905736; Colle: AGS-1904809; Oue and Kollias: AGS-1841215 and 2113070) and the National Aeronautics and Space Administration (Yuter: 80NSSC19K0354). We thank Dr. Robert M. Rauber and two anonymous reviewers for fruitful comments and suggestions. We also thank the students of the School of Marine and Atmospheric Sciences, Stony Brook University, who performed sounding observations.

Data availability statement. KASPR and sounding data used in this study are available at Stony Brook University Academic Commons Repository (<https://commons.library.stonybrook.edu/somasdata/17>). Those data collected under IMPACTS are also available at the NASA Global Hydrometeorology Resource Center (GHRC) DAAC system (<https://doi.org/10.5067/IMPACTS/RADAR/DATA101>; <https://doi.org/10.5067/IMPACTS/SOUNDING/DATA301>).

APPENDIX

Contribution of Turbulence to Doppler Spectrum Width

There are six major Doppler spectral broadening mechanisms that contribute to the measured spectrum width σ_{tot} (Doviak and Zrníc 2006): dispersion of hydrometeor fall speed σ_{psd} , turbulence σ_{tur} , mean horizontal wind shear σ_{shr} , crosswind σ_{crs} , antenna motion σ_{ant} , and parameters related to the particle orientation (including canting, horizontal orientation, wobbling, and oscillation of shape; Dunnavan 2021) σ_{ori} . Those contributions can be written as

$$\sigma_{\text{tot}} = \sqrt{\sigma_{\text{psd}}^2 + \sigma_{\text{tur}}^2 + \sigma_{\text{shr}}^2 + \sigma_{\text{crs}}^2 + \sigma_{\text{ant}}^2 + \sigma_{\text{ori}}^2}. \quad (\text{A1})$$

To simplify, the contributions of σ_{ant} and σ_{ori} are ignored, assuming that they are negligible compared to the other terms. Moreover, for the VPT measurements, σ_{shr} and σ_{crs} can also be negligible compared to σ_{psd} and σ_{tur} . The value of σ_{shr} in Eq. (A1) differs from the original surveillance-scan form proposed by Doviak and Zrníc (2006) because we neglect possible contributions from vertical wind shear across the sampling volume; only the horizontal wind shear component is considered here. For the VPT measurements in this study, we consider the σ_{psd} and σ_{tur} to evaluate the contributions to σ_{tot} as

$$\sigma_{\text{tot}} = \sqrt{\sigma_{\text{psd}}^2 + \sigma_{\text{tur}}^2}. \quad (\text{A2})$$

In the case of VPT measurements, σ_{tur} in Eq. (A2) can represent the dispersion of radial velocities within the sampling volume owing to turbulent structures and/or horizontal gradients in coherent vertical structures. To estimate general σ_{psd} for the present cases, Fig. A1a shows a frequency distribution of SW versus reflectivity from the KASPR VPT measurements collected during the selected four events in this study. In this figure, we assume that σ_{psd} can be correlated with reflectivity statistically. The SW with the maximum frequency at each reflectivity bin increased with reflectivity. This can represent statistical σ_{psd} associated with reflectivity. For the four cases, which are stratiform snow events, radar reflectivity generally increases with decreasing height, suggesting that hydrometeor particles generally grow downward. As the particle size distribution broadens with increasing reflectivity, σ_{psd} , which is attributed to the spread of particle fall speeds in the radar resolution volume can also increase. The SW with maximum frequency is generally less than 0.2 m s^{-1} . Figure A1b shows vertical frequency distribution of the SW. The SW with maximum frequency increases downward and is generally less than 0.2 m s^{-1} .

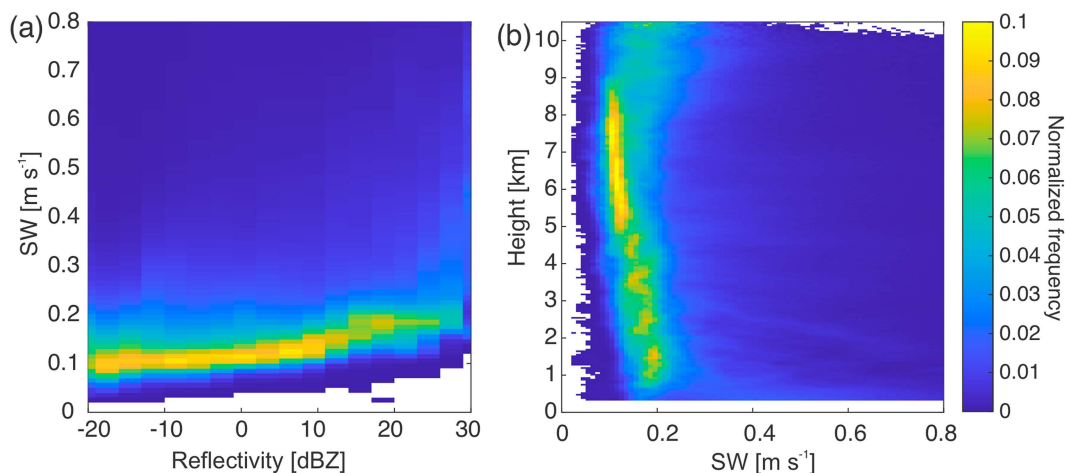


FIG. A1. (a) Frequency distribution of SW vs reflectivity from the KASPR VPT measurements collected during the four events. The color shade represents the frequency normalized every 2 dBZ from -20 dBZ . (a) Frequency by altitude distribution of SW. Color shade represents the frequency normalized at each radar range gate (every 15 m).

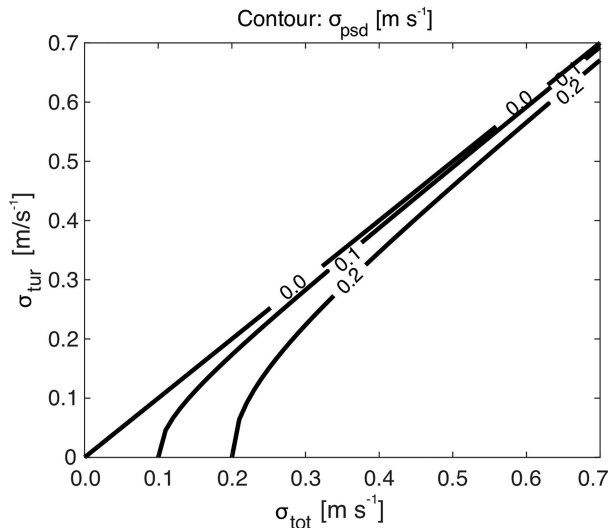


FIG. A2. σ_{tur} vs σ_{tot} diagram with corresponding σ_{psd} based on Eq. (A2).

Figure A2 shows the relationship of Eq. (A2) to represent the contributions of σ_{psd} and σ_{tur} to σ_{tot} . At σ_{tot} (observed SW) = 0.3 m s^{-1} with $\sigma_{\text{psd}} = 0.2 \text{ m s}^{-1}$, σ_{tur} is approximately 0.2 m s^{-1} , comparable with σ_{psd} . For $\sigma_{\text{tot}} > 0.35 \text{ m s}^{-1}$ with $\sigma_{\text{psd}} = 0.2 \text{ m s}^{-1}$, $\sigma_{\text{tur}} > \sigma_{\text{psd}}$, indicating that σ_{tur} can be a primary contribution to the observed SW. We use $\sigma_{\text{tot}} = 0.4 \text{ m s}^{-1}$ for the threshold of observed SW to classify detected updraft regions related to turbulence. When we compared statistics using a threshold of $\sigma_{\text{tot}} = 0.4 \text{ m s}^{-1}$ and a threshold of 0.5 m s^{-1} , the medians of duration and vertical extent for URSWHI and URSWLO did not change much (less than 1 s and less than 15 m, respectively). The medians of reflectivity and upward motion slightly increased as we expected; median reflectivity for URSWHI increased by $\sim 0.5 \text{ dB}$ and that for URSWLO increased by $\sim 2 \text{ dB}$, and median upward motions for both URSWHI and URSWLO increased by less than 0.05 m s^{-1} .

REFERENCES

- Benjamin, S. G., and Coauthors, 2016: A North American hourly assimilation and model forecast cycle: The Rapid Refresh. *Mon. Wea. Rev.*, **144**, 1669–1694, <https://doi.org/10.1175/MWR-D-15-0242.1>.
- Bluestein, H. B., 1993: *Observations and Theory of Weather Systems*. Vol. II, *Synoptic-Dynamic Meteorology in Midlatitudes*. Oxford University Press, 608 pp.
- Bosart, L. F., and F. Sanders, 1986: Mesoscale structure in the megapolitan snowstorm of 11–12 February 1983. Part III: A large-amplitude gravity wave. *J. Atmos. Sci.*, **43**, 924–939, [https://doi.org/10.1175/1520-0469\(1986\)043<0924:MSITMS>2.0.CO;2](https://doi.org/10.1175/1520-0469(1986)043<0924:MSITMS>2.0.CO;2).
- Boucher, R. J., R. Wexler, D. Atlas, and R. M. Lhermitte, 1965: Mesoscale wind structure revealed by Doppler radar. *J. Appl. Meteor.*, **4**, 590–597, [https://doi.org/10.1175/1520-0450\(1965\)004<0590:MWSRBD>2.0.CO;2](https://doi.org/10.1175/1520-0450(1965)004<0590:MWSRBD>2.0.CO;2).
- Browning, K. A., and R. Wexler, 1968: The determination of kinematic properties of a wind field using Doppler radar. *J. Appl. Meteor.*, **7**, 105–113, [https://doi.org/10.1175/1520-0450\(1968\)007<0105:TDOKPO>2.0.CO;2](https://doi.org/10.1175/1520-0450(1968)007<0105:TDOKPO>2.0.CO;2).
- Bryan, G. H., and J. M. Fritsch, 2000: Moist absolute instability: The sixth static stability state. *Bull. Amer. Meteor. Soc.*, **81**, 1207–1230, [https://doi.org/10.1175/1520-0477\(2000\)081<1287:MAITSS>2.3.CO;2](https://doi.org/10.1175/1520-0477(2000)081<1287:MAITSS>2.3.CO;2).
- Byrd, G. P., 1989: A composite analysis of winter season overrunning precipitation bands over the southern plains of the United States. *J. Atmos. Sci.*, **46**, 1119–1132, [https://doi.org/10.1175/1520-0469\(1989\)046<1119:ACAOWS>2.0.CO;2](https://doi.org/10.1175/1520-0469(1989)046<1119:ACAOWS>2.0.CO;2).
- Colle, B. A., D. Stark, and S. E. Yuter, 2014: Surface microphysical observations within East Coast winter storms on Long Island, New York. *Mon. Wea. Rev.*, **142**, 3126–3146, <https://doi.org/10.1175/MWR-D-14-00035.1>.
- Cooper, K. B., and G. Chattopadhyay, 2014: Submillimeter-wave radar: Solid-state system design and applications. *IEEE Microwave Mag.*, **15**, 51–67, <https://doi.org/10.1109/MMM.2014.2356092>.
- Crawford, A. D., E. A. P. Schreiber, N. Sommer, M. C. Serreze, J. C. Stroeve, and D. G. Barber, 2021: Sensitivity of Northern Hemisphere cyclone detection and tracking results to fine spatial and temporal resolution using ERA5. *Mon. Wea. Rev.*, **149**, 2581–2598, <https://doi.org/10.1175/MWR-D-20-0417.1>.
- Doviak, R. J., and D. S. Zrnić, 2006: *Doppler Radar and Weather Observations*. 2nd ed. Academic Press, 562 pp.
- Dunnavan, E. L., 2021: How snow aggregate ellipsoid shape and orientation variability affects fall speed and self-aggregation rates. *J. Atmos. Sci.*, **78**, 51–73, <https://doi.org/10.1175/JAS-D-20-0128.1>.
- Ganetis, S. A., B. A. Colle, S. E. Yuter, and N. P. Hoban, 2018: Environmental conditions associated with observed snow-band structures within northeast U.S. winter storms. *Mon. Wea. Rev.*, **146**, 3675–3690, <https://doi.org/10.1175/MWR-D-18-0054.1>.
- Hersbach, H., and Coauthors, 2020: The ERA5 global reanalysis. *Quart. J. Roy. Meteor. Soc.*, **146**, 1999–2049, <https://doi.org/10.1002/qj.3803>.
- Jurewicz, M. L., Sr., and M. S. Evans, 2004: A comparison of two banded, heavy snowstorms with very different synoptic settings. *Wea. Forecasting*, **19**, 1011–1028, <https://doi.org/10.1175/WAF-823.1>.
- Keeler, J. M., B. F. Jewett, R. M. Rauber, G. M. McFarquhar, R. M. Rasmussen, L. Xue, C. Liu, and G. Thompson, 2016a: Dynamics of cloud-top generating cells in winter cyclones. Part I: Idealized simulations in the context of field observations. *J. Atmos. Sci.*, **73**, 1507–1527, <https://doi.org/10.1175/JAS-D-15-0126.1>.
- , —, —, —, —, —, —, and —, 2016b: Dynamics of cloud-top generating cells in winter cyclones. Part II: Radiative and instability forcing. *J. Atmos. Sci.*, **73**, 1529–1553, <https://doi.org/10.1175/JAS-D-15-0127.1>.
- , —, —, —, —, —, —, and —, 2017: Dynamics of cloud-top generating cells in winter cyclones. Part III: Shear and convective organization. *J. Atmos. Sci.*, **74**, 2879–2897, <https://doi.org/10.1175/JAS-D-16-0314.1>.
- Kollias, P., N. Bharadwaj, K. Widener, I. Jo, and K. Johnson, 2014: Scanning ARM cloud radars. Part I: Operational sampling strategies. *J. Atmos. Oceanic Technol.*, **31**, 569–582, <https://doi.org/10.1175/JTECH-D-13-00044.1>.
- , E. Luke, M. Oue, and K. Lamer, 2020: Agile adaptive radar sampling of fast-evolving atmospheric phenomena guided by

- satellite imagery and surface cameras. *Geophys. Res. Lett.*, **47**, e2020GL088440, <https://doi.org/10.1029/2020GL088440>.
- Kumjian, M. R., and K. A. Lombardo, 2017: Insights into the evolving microphysical and kinematic structure of northeastern U.S. winter storms from dual-polarization Doppler radar. *Mon. Wea. Rev.*, **145**, 1033–1061, <https://doi.org/10.1175/MWR-D-15-0451.1>.
- , S. A. Rutledge, R. M. Rasmussen, P. C. Kennedy, and M. Dixon, 2014: High-resolution polarimetric radar observations of snow-generating cells. *J. Appl. Meteor. Climatol.*, **53**, 1636–1658, <https://doi.org/10.1175/JAMC-D-13-0312.1>.
- , D. M. Tobin, M. Oue, and P. Kollias, 2020: Microphysical insights into ice pellet formation revealed by fully polarimetric Ka-band Doppler radar. *J. Appl. Meteor. Climatol.*, **59**, 1557–1580, <https://doi.org/10.1175/JAMC-D-20-0054.1>.
- Lackmann, G. M., and G. Thompson, 2019: Hydrometeor lofting and mesoscale snowbands. *Mon. Wea. Rev.*, **147**, 3879–3899, <https://doi.org/10.1175/MWR-D-19-0036.1>.
- Lamer, K., M. Oue, A. Battaglia, R. J. Roy, K. B. Cooper, R. Dhillon, and P. Kollias, 2021: Multifrequency radar observations of clouds and precipitation including the G-band. *Atmos. Meas. Tech.*, **14**, 3615–3629, <https://doi.org/10.5194/amt-14-3615-2021>.
- Markowski, P. M., and Y. P. Richardson, 2010: *Mesoscale Meteorology in Midlatitudes*. Wiley-Blackwell, 424 pp.
- McMurdie, L. A., and Coauthors, 2022: Chasing snowstorms: The Investigation of Microphysics and Precipitation for Atlantic Coast-Threatening Snowstorms (IMPACTS) campaign. *Bull. Amer. Meteor. Soc.*, **103**, E1243–E1269, <https://doi.org/10.1175/BAMS-D-20-0246.1>.
- Molthan, A. L., B. A. Colle, S. E. Yuter, and D. Stark, 2016: Comparisons of modeled and observed reflectivities and fall speeds for snowfall of varied riming degrees during winter storms on Long Island, New York. *Mon. Wea. Rev.*, **144**, 4327–4347, <https://doi.org/10.1175/MWR-D-15-0397.1>.
- Morales, R. F., Jr., 2008: The historic Christmas 2004 south Texas snow event: Diagnosis of the heavy snow band. *Natl. Wea. Dig.*, **32**, 135–152.
- Naeger, A. R., B. A. Colle, and A. Molthan, 2017: Evaluation of cloud microphysical schemes for a warm frontal snowband during the GPM Cold Season Precipitation Experiment (GCPEX). *Mon. Wea. Rev.*, **145**, 4627–4650, <https://doi.org/10.1175/MWR-D-17-0081.1>.
- , —, N. Zhou, and A. Molthan, 2020: Evaluating warm and cold rain processes in cloud microphysical schemes using OLYMPLEX field measurements. *Mon. Wea. Rev.*, **148**, 2163–2190, <https://doi.org/10.1175/MWR-D-19-0092.1>.
- Novak, D. R., L. F. Bosart, D. Keyser, and J. S. Waldstreicher, 2004: An observational study of cold season-banded precipitation in northeast U.S. cyclones. *Wea. Forecasting*, **19**, 993–1010, <https://doi.org/10.1175/815.1>.
- , B. A. Colle, and S. E. Yuter, 2008: High-resolution observations and model simulations of the life cycle of an intense mesoscale snowband over the northeastern United States. *Mon. Wea. Rev.*, **136**, 1433–1456, <https://doi.org/10.1175/2007MWR2233.1>.
- , —, and A. R. Aiyer, 2010: Evolution of mesoscale precipitation band environments within the comma head of northeast U.S. cyclones. *Mon. Wea. Rev.*, **138**, 2354–2374, <https://doi.org/10.1175/2010MWR3219.1>.
- Oue, M., P. Kollias, E. P. Luke, and A. Ryzhkov, 2017: A new Ka-band scanning radar facility: Polarimetric and Doppler spectra measurements of snow events. *2017 Fall Meeting*, New Orleans, Amer. Geophys. Union, Abstract A31G-2270, <https://agu.confex.com/agu/fm17/meetingapp.cgi/Paper/276182>.
- , —, S. Y. Matrosov, A. Battaglia, and A. V. Ryzhkov, 2021: Analysis of the microphysical properties of snowfall using scanning polarimetric and vertically pointing multi-frequency Doppler radars. *Atmos. Meas. Tech.*, **14**, 4893–4913, <https://doi.org/10.5194/amt-14-4893-2021>.
- Petterssen, S., 1956: *Motion and Motion Systems*. Vol. I, *Weather Analysis and Forecasting*, McGraw-Hill, 428 pp.
- Plummer, D. M., G. M. McFarquhar, R. M. Rauber, B. F. Jewett, and D. C. Leon, 2014: Structure and statistical analysis of the microphysical properties of generating cells in the comma-head region of continental winter cyclones. *J. Atmos. Sci.*, **71**, 4181–4203, <https://doi.org/10.1175/JAS-D-14-0100.1>.
- , —, —, —, and —, 2015: Microphysical properties of convectively generated fall streaks within the stratiform comma head region of continental winter cyclones. *J. Atmos. Sci.*, **72**, 2465–2483, <https://doi.org/10.1175/JAS-D-14-0354.1>.
- Protat, A., and C. R. Williams, 2011: The accuracy of radar estimates of ice terminal fall speed from vertically pointing Doppler radar measurements. *J. Appl. Meteor. Climatol.*, **50**, 2120–2138, <https://doi.org/10.1175/JAMC-D-10-05031.1>.
- Rauber, R. M., and Coauthors, 2014: Stability and charging characteristics of the comma head region of continental winter cyclones. *J. Atmos. Sci.*, **71**, 1559–1582, <https://doi.org/10.1175/JAS-D-13-0253.1>.
- , S. M. Ellis, J. Vivekanandan, J. Stith, W.-C. Lee, G. M. McFarquhar, B. F. Jewett, and A. Janiszewski, 2017: Finescale structure of a snowstorm over the northeastern United States: A first look at high-resolution HIAPER cloud radar observations. *Bull. Amer. Meteor. Soc.*, **98**, 253–269, <https://doi.org/10.1175/BAMS-D-15-00180.1>.
- Reuter, G. W., and M. K. Yau, 1990: Observations of slantwise convective instability in winter cyclones. *Mon. Wea. Rev.*, **118**, 447–458, [https://doi.org/10.1175/1520-0493\(1990\)118<0447:OOSCI>2.0.CO;2](https://doi.org/10.1175/1520-0493(1990)118<0447:OOSCI>2.0.CO;2).
- Rosenow, A. A., D. M. Plummer, R. M. Rauber, G. M. McFarquhar, B. F. Jewett, and D. Leon, 2014: Vertical velocity and physical structure of generating cells and convection in the comma head region of continental winter cyclones. *J. Atmos. Sci.*, **71**, 1538–1558, <https://doi.org/10.1175/JAS-D-13-0249.1>.
- , R. M. Rauber, B. F. Jewett, G. M. McFarquhar, and J. M. Keeler, 2018: Elevated potential instability in the comma-head: Distribution and development. *Mon. Wea. Rev.*, **146**, 1259–1278, <https://doi.org/10.1175/MWR-D-17-0283.1>.
- Schmidt, J. M., and Coauthors, 2012: Radar observations of individual rain drops in the free atmosphere. *Proc. Natl. Acad. Sci. USA*, **109**, 9293–9298, <https://doi.org/10.1073/pnas.111776109>.
- Schultz, D. M., and P. N. Schumacher, 1999: The use and misuse of conditional symmetric instability. *Mon. Wea. Rev.*, **127**, 2709–2732, [https://doi.org/10.1175/1520-0493\(1999\)127<2709:TUAMOC>2.0.CO;2](https://doi.org/10.1175/1520-0493(1999)127<2709:TUAMOC>2.0.CO;2).
- , and J. A. Knox, 2007: Banded convection caused by frontogenesis in a conditionally, symmetrically, and inertially unstable environment. *Mon. Wea. Rev.*, **135**, 2095–2110, <https://doi.org/10.1175/MWR3400.1>.
- Stark, D., B. A. Colle, and S. E. Yuter, 2013: Observed microphysical evolution for two East Coast winter storms and the associated snow bands. *Mon. Wea. Rev.*, **141**, 2037–2057, <https://doi.org/10.1175/MWR-D-12-00276.1>.
- Syrett, W. J., B. A. Albrecht, and E. E. Clothiaux, 1995: Vertical cloud structure in a midlatitude cyclone from a 94-GHz radar. *Mon. Wea. Rev.*, **123**, 3393–3407, [https://doi.org/10.1175/1520-0493\(1995\)123<3393:VCSIAM>2.0.CO;2](https://doi.org/10.1175/1520-0493(1995)123<3393:VCSIAM>2.0.CO;2).

- Trapp, J. R., D. M. Schultz, A. V. Ryzhkov, and R. L. Holle, 2001: Multiscale structure and evolution of an Oklahoma winter precipitation event. *Mon. Wea. Rev.*, **129**, 486–501, [https://doi.org/10.1175/1520-0493\(2001\)129<0486:MSAEOA>2.0.CO;2](https://doi.org/10.1175/1520-0493(2001)129<0486:MSAEOA>2.0.CO;2).
- Wexler, R., A. C. Chmela, and G. M. Armstrong, 1967: Wind field observations by Doppler radar in a New England snowstorm. *Mon. Wea. Rev.*, **95**, 929–935, [https://doi.org/10.1175/1520-0493\(1967\)095<0929:WFOBDR>2.3.CO;2](https://doi.org/10.1175/1520-0493(1967)095<0929:WFOBDR>2.3.CO;2).
- Xu, Q., 1992: Formation and evolution of frontal rainbands and geostrophic potential vorticity anomalies. *J. Atmos. Sci.*, **49**, 629–648, [https://doi.org/10.1175/1520-0469\(1992\)049<0629:FAEOFR>2.0.CO;2](https://doi.org/10.1175/1520-0469(1992)049<0629:FAEOFR>2.0.CO;2).
- Zhang, F., S. E. Koch, C. A. Davis, and M. L. Kaplan, 2001: Wavelet analysis and the governing dynamics of a large-amplitude gravity wave event along the East Coast of the United States. *Quart. J. Roy. Meteor. Soc.*, **127**, 2209–2245, <https://doi.org/10.1002/qj.49712757702>.
- , C. Synder, and R. Rotunno, 2003: Effects of moist convection on mesoscale predictability. *J. Atmos. Sci.*, **60**, 1173–1185, [https://doi.org/10.1175/1520-0469\(2003\)060<1173:EOMCOM>2.0.CO;2](https://doi.org/10.1175/1520-0469(2003)060<1173:EOMCOM>2.0.CO;2).